Indocyanine-green fluorescence imaging to detect anastomotic insufficiency after esophagectomy
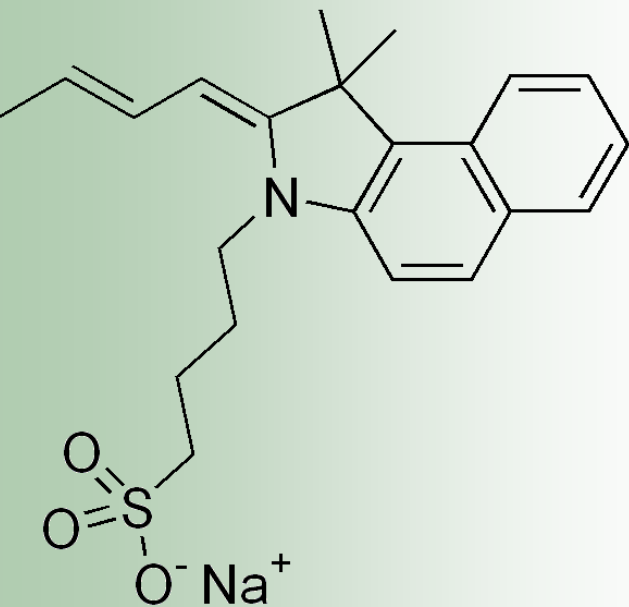
Development of models, methods and instrumentation

Love Kildetoft

Thesis submitted for the degree of master of science

Supervised by Anna-Lena Sahlberg and Adam Zeyara

Project duration: 6 months

Indocyanine-green fluorescence imaging to detect anastomotic insufficiency after esophagectomy

Development of models, methods and instrumentation

by Love Kildetoft

LUND
UNIVERSITY

Abstract

This research project is concerned with the development of simulation models and image analysis algorithms, as well as instrumentation for characterizing anastomotic leakages after a patient has undergone surgery for esophageal cancer. Anastomotic leakage is a high-incidence complication after esophagectomy, a surgical procedure for esophageal cancer. In an esophagectomy, the cancerous part of the esophagus is resected, and an artificial counterpart is created by stretching the ventricle. After sewing these two tissues together, there is a high chance of the stitches rupturing due to poor healing, something which in turn arises from poor and complicated blood perfusion in the area. This thesis work aims to utilize indocyanine green, a fluorescent molecule which binds to plasma proteins in blood. By imaging the anastomotic area after an ICG injection and illuminating it with a fitting excitation light source, one may be able to determine areas of poor perfusion by studying the time evolution of the fluorescence signal. The algorithms developed in this thesis achieve this in two different ways: purely by calculating the time to the fluorescence maximum for each pixel, and also by numerically approximating the time-intensity derivative. These are tested on the aforementioned Monte-Carlo simulation model, as well as on tissue phantoms, and finally in-vivo in a porcine model. The results indicate that the algorithms perform well and reveal relevant features in the fluorescence signal, in all cases. The porcine measurements prove highly useful to show the benefits and disadvantages of each algorithm, and the conclusion is that they should likely be used together to provide physicians with a full picture of the perfusion. Finally, an outlook on how this could be incorporated into a gastroscopy setup is provided, something which was discussed during this thesis work but never fully realized.

Populärvetenskaplig sammanfattning på svenska

De flesta av oss har sorgligt nog en personlig anknytning till sjukdomen *cancer*. För en god prognos är det helt avgörande att sjukdomen upptäcks i ett tidigt skede så att behandling kan påbörjas. När det gäller cancer i matstrupen (*esofaguscancer*) är detta sällan fallet och prognosen är därför ofta mycket dålig för den drabbade, med en generell överlevnadsgrad på ca 10-20% efter fem år.[10]

Esofaguscancer behandlas operativt i de fall där det är möjligt, något som förbättrar prognosen för patienten avsevärt. Den operativa behandlingen är vanligtvis en så kallad *esofagektomi*, vid vilken en stor del av matstrupen opereras bort och rekonstrueras genom att ansluta magsäcken till det som återstår av esofagus. Prognosen efter detta är generellt sett god för patienten, då denne både blir fri från sin cancer samt kan äta och svälja normalt en tid efter ingreppet.[1]

Trots detta är proceduren inte riskfri. Området där matstrupen anslutits till magsäcken är generellt mycket känsligt för anomalier i blodflödet, som i sin tur påverkar läkningen. Om den kirurgiska anslutningen inte läker samman ordentligt löper patienten stor risk att drabbas av såkallad *anastomosinsufficiens*, där den kirurgiska anslutningen brister. Detta är en fruktad komplikation, då den både är svår för läkare att förutse samt, om den lämnas obehandlad, i princip alltid innebär en dödlig utgång då patienten snabbt utvecklar kraftig inflammation och drabbas av blodförgiftning.[1] Detta sker i ca 15-25% av de fall där patienten genomgått behandling i Sverige, en förhållandevis hög frekvens.[21]

Att upptäcka och förutse stundande anastomosinsufficiens är svårt, då det kräver en invasiv undersökning. Ytterliggare är det inte trivialt att mäta blodflödet i anastomosområdet, och således är oftast problemet sedan länge uppkommet när en läkare upptäcker det.[1]

I detta arbete ämnar vi att använda *fluorescensdiagnostik* för att karakterisera blodflödet i den rekonstruerade esofagus efter en patient genomgått esofagektomi. Fluorescerande ämnen återfinns dagligen i bland annat lysrör[30], drinken gin & tonic [41] samt i vissa typer av tvättmedel[40]. Begreppet innebär kort sagt att ett ämne börjar lysa om det belyses med en viss våglängd, med en annan ton än belysningskällan. Denna fluorescensvåglängd är i de flesta fall längre än den ingående, men motsatsen förekommer också.

Indocyaningrönt (ICG) är ett fluorescerande protein som kemiskt binder till de plasmaproteiner som förekommer i blod.[32] Genom att injicera detta i en patients blodflöde och med hjälp av ett gastroskop belysa anastomosområdet ämnar vi att mäta den tid det tar att få en fluorescenssignal, i den matris av pixlar som fås när en avbildar något fotografiskt. Genom att visualisera tidsförloppet i varje pixel kommer detta ge en bild av hur snabbt ICG, och således blod levereras i olika delar av den rekonstruerade esofagus. Genom att snabbt och regelbundet genomföra sådana mätningar efter genomgången operation är förhoppningen att detta skall avslöja blodflödesfokaliteter i god tid innan anastomosinsufficiens uppstår.

Projektet innefattar utveckling av simuleringar samt bildanalysalgoritmer, och ex- samt in-vivo experiment för att utvärdera dessa. Ytterliggare presenteras en utblick mot hur ett gastroskopiinstrument för dessa mätningar kan byggas. ICG fluorescerar infrarött, vid ca 800 nm[32] och gastroskopet behöver därför utökas både med en kamera som kan se detta ljus samt en ljuskälla för att excitera det. De flesta industriellt tillverkade gastroskop är utrustade med en arbetskanal där olika typer av instrument kan föras in. Tanken är att denna skulle kunna användas för att leverera samt insamla ljus i området.

Den höga frekvensen av anastomosinsufficiens har digra konsekvenser både för de efterlevande samt samhället, då sjukhusutgifter även ökar kraftigt både i fallet att patienten dör och fallet att den överlever. Siffror från Skånes universitetssjukhus uppskattar kostnaden av varje inträffat fall av anastomosinsufficiens till ca en miljon kronor oavsett utgången för patienten. [25]

Målet är att presentera en mer eller mindre komplett lösning för att karaktärisera upptag av indocyaningrönt i esofagus, som är förhållandevis billig att tillverka samt enbart kräver befintliga komponenter. Förhoppningen är att detta projekt skall utgöra det första steget mot ett instrument som kan användas kliniskt, för att minska

den höga frekvensen anastomosläckage och således lidandet för alla inblandade.

Acknowledgements

Contents

List of Figures

List of Tables

Chapter 1

Introduction

This thesis deals with the development of a fluorescence imaging technique to alleviate the early detection of poor blood perfusion as well as complications after a patient has undergone surgical treatment for esophageal cancer. In this chapter, the main motivation and aims behind the work are described.

1.1   Background and motivation

Esophageal cancer is a collective term, which denotes tumours occurring in the *esophagus* - a long and narrow muscular tube which connects the pharynx with the stomach. [9] Its main function is to allow the ingestion and swallowing of food and nutrition.

The mortality rate of patients with esophageal cancer is extremely high in comparison to several other cancers, approaching 90% when considering patient survival in five years after their initial diagnosis. [33] Part of this can be attributed to clear symptoms such as difficulties swallowing only occurring at an advanced stage of the tumour growth, at which metastases may already be present throughout the body. The detection of an esophageal tumour at earlier stages involves invasive procedures such as gastroscopy and is usually not performed unless the disease is highly suspected in the patient. [33]

Figure 1.1: An illustration of the esophagectomy procedure[11]

As a result of this, esophageal cancer is often treated surgically through a procedure known as an *esophagectomy*. Esophagectomies involve a partial or most often, full resection of the esophagus, which is then reconstructed using ventricular (stomach) tissue. [1] The ventricle is stretched and surgically connected to the remainder of the esophagus. The surgical connection itself is denoted an *anastomosis*.

As with any surgery, there are many complications which may arise after an esophagectomy. One of these is so-called *anastomotic insufficiency*, in which the aforementioned anastomosis fails and subsequently ruptures. If left without surgical intervention, this is a catastrophic complication for the patient which may lead to multiple organ failure and even death. [1] What follows are dire consequences: higher rates of in-hospital mortality, suffering for the ones who survive the deceased, as well as excessive health care costs. [1]

Anastomotic insufficiency often occurs as a result of ischemia - poor blood perfusion in the ventricular tube. [1] The perfusion in this region is very poor, especially in the area directly below the anastomosis as it is supplied by a single artery after an esophagectomy has been performed. [9] As such, this area is highly sensitive to discrepancies in blood perfusion. This can ultimately lead to poor healing and subsequently, anastomotic insufficiency and leakage.
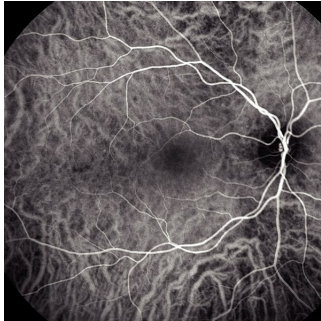
Figure 1.2: An angiographic ICG-fluorescence image of the human eye, clearly displaying the choroidal arteries[9] where blood is flowing.[14]

Fluorescence imaging is a standard technique in several medical disciplines and has been for many years. [2] Such techniques rely on *fluorophores*, fluorescent molecules which emit light after having been excited. If a fluorophore is excited by illumination with another source of light, the fluorescence signal is always longer in wavelength than the excitation source. [34] If this shift is large enough, one may obtain a very clear contrast between signals from the light source and the fluorescence signal. [2]

Indocyanine-green [ICG] is a green fluorescent dye, developed by Kodak during the second world war and used for medical purposes since the late 1950s. [26] It has a peak spectral absorption at around 800 nm and as such fluoresces in the near-infrared. Clinically, its properties are excellent as it is nontoxic in reasonable doses and it is cleared by the liver and bile in minutes following injection. [32]

ICG chemically binds to albumin and other common proteins found in human blood plasma. As such the fluorescence signal is often used for *angiography*, the visualization of blood flow through arteries and veins.[2] These techniques however only display that blood is flowing and serve a qualitative purpose. To make quantitative predictions, such as deriving perfusion speeds in different parts of the image one must apply further mathematical and statistical analysis on the optical image. This is the case if one for example intends to predict the healing of the anastomosis after an esophagectomy: as the anastomosis is supplied with blood by several arteries, the unprocessed fluorescence image will display this. It will however not show if there are any discrepancies in the perfusion speed of the blood, the factor which mainly contributes to poor healing and subsequent anastomotic insufficiency.

1.2   Aim of this work

This work strives towards developing a complete fluorescence imaging toolkit to quantify ICG-fluorescence in the context of esophagectomies.

The work includes the following:

- The development of a Monte-Carlo simulation model for ICG-fluorescence in the context of esophagectomies

- Algorithm development for the quantification of the ICG fluorescence signal, specifically to characterise blood perfusion

- Ex- and in-vivo measurements of ICG-fluorescence, to test the image analysis algorithms

- Discussion around the required instrumentation to perform these measurements, as well as an outlook toward how this toolkit could be extended into a full endoscopic instrument.

Chapter 2

Theory of light-matter interaction in biological tissue

As this thesis presents work that is highly interdisciplinary it is worth dividing the usual theory chapter into two parts. In this chapter the relevant theory from physics is described, starting from the interaction between light and matter. In chapter 3, the relevant medical background is described.

2.1 Energy states and transitions in molecules

When light of high enough energy is incident on a molecular compound it excites the molecules into higher energy states. As a consequence of quantum mechanics, these states are discrete and characterized by the difference in energy between them. [34] For matter to undergo excitation in this way, the energy of each incident photon must either exceed or be equal to the energy difference between the ground state and the excited state. Do note that if the photon energy is greater than the energy difference between the ground state and a certain excited state, the molecule may be excited to a higher energy state or undergo ionization.

The energy of a photon of wavelength λ is given

$$E_{ph} = \frac{hc}{\lambda} \tag{2.1}$$

where c is the speed of light in a medium (with a certain refractive index) and h is *Plancks constant*. [34]

The energy structure of a molecule is usually well described by the so-called *Born-Oppenheimer* approximation [36]

$$E_{total} = E_{electronic} + E_{vibrational} + E_{rotational} \tag{2.2}$$

The total energy of a molecule can as such be separated into three subsequent parts. The levels are discrete according to quantum mechanics and each type of transition is accompanied by its own quantum number. We refrain from exact expressions for these here as they are of little relevance to this thesis, but they can be found in almost any graduate-level textbook on atomic and

Figure 2.1: An illustration of the different types of energy transitions present in a molecule, and their respective energy ranges. [16]

molecular physics (see for example *Atomic and Molecular Spectroscopy* by Svanberg. [36])

Given two energy levels E_1 and E_2, it is regardless of their nature required that

$$E_{ph} = |E_2 - E_1| \qquad (2.3)$$

for the molecule to undergo excitation from E_1 to E_2 by the absorption of a photon.

Matter, which has been excited will eventually decay back into its ground state resulting in the emission of energy. In this process, it may either undergo a *radiative* transition in which the energy is emitted as a photon of energy ΔE or it may undergo a *non-radiative* transition, for example by transfer to other molecules in the compound. The non-radiative process in question is dependent on the molecular compound.
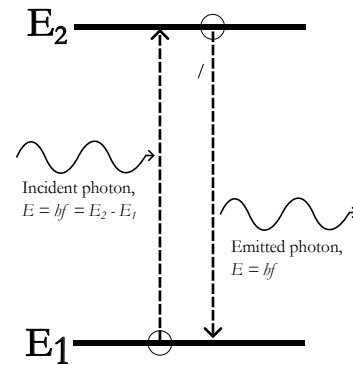
Figure 2.2: An illustration of the absorption and spontaneous emission of a photon between two energy levels in for example a molecule.

2.2 Photoluminescence: fluorescence and phosphorescence

If the molecule in question has a decay scheme in which it undergoes both radiative and non-radiative processes after excitation by a photon, it is denoted *photoluminescent*. This subsequently leads to the emission of photons of longer wavelengths, and thus lower energy (see eq. (2.1)) than that of the incident photons (it is worth noting that there exist cases where the contrary is true, and the output wavelength is blue-shifted instead. These are however not described in this section as they are not relevant to the scope of this project.). This wavelength shift is commonly denoted the *Stokes shift*.[7]

The lifetime of the transitions depends on their so-called *spin multiplicity*, a purely quantum mechanical effect. [34] Here, only a brief outline is provided and the reader is referred to for example *Atomic Physics*[15] by C. J. Foot for a thorough description.

Due to their leptonic nature, electrons always have a spin of $s = \pm\frac{1}{2}$. [15] The total spin S of an atom is given [36]

$$S = \sum_i s_i \qquad (2.4)$$

where $s_{i,n}$ denotes the spin of electron i.
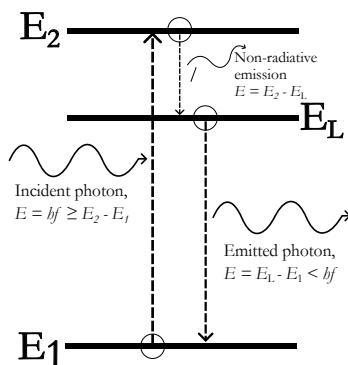
Figure 2.3: An illustration of general photoluminescence, in which there are one or several intermediate non-radiative transitions, resulting in the emission of a photon of longer wavelength than the incoming photon.

The spin multiplicity is in turn given by

$$m = 2S + 1 \qquad (2.5)$$

Each energy level in an atom will have a certain multiplicity as it contains a certain number of electrons. As a consequence of quantum mechanics, transitions between energy levels of equal multiplicity are favored and as such more probable than transitions between states of different multiplicity. Such transitions are called *spin-forbidden* whereas transitions between states of equal multiplicity are *spin-allowed*. [15]

If the radiative transition in a photoluminescent molecule is spin-allowed, it generally happens quickly after excitation as it has a higher probability. Such molecules are denoted *fluorescent*, and the process itself is denoted *fluorescence*. On the contrary, if the transition is spin-forbidden, the process takes much longer and light emission is not immediately observed. This form of photoluminescence is called *phosphorescence*. [34]

The fluorescence cross-section of a certain fluorescent molecule (henceforth denoted *fluorophore*) can be defined as [7]

$$\sigma_{fluor} = \eta \sigma_{abs} \frac{f_{fluor}}{f_{abs}} \tag{2.6}$$

where σ_{abs} is the corresponding absorption cross-section, η is the quantum efficiency (i.e. the ratio of the number of fluorescence events per second over the number of absorption events per second) and f_{fluor} and f_{abs} are the frequencies of the emitted and incident light respectively.

The lifetime τ of a fluorophore, i.e the average time until fluorescence is no longer observed following excitation is given by [7]

$$\tau = \frac{\eta}{r_{fluor}} \tag{2.7}$$

where r_{fluor} is the fluorescence rate constant.

The lifetime in itself is highly affected by a process known as *quenching* in which the quantum yield is lowered due to other means of de-excitation being favoured over the fluorescence transition. [7] The amount of quenching depends highly on the surroundings of the fluorophore. For example, a high amount of quenching is obtained if the fluorophore is diluted in a molecular compound in which collisional energy transfer is probable. [7]

The *quenched quantum yield* is given by

$$\eta_q = \frac{\eta}{1 + \tau r_q N_q} \tag{2.8}$$

where r_q is the quenching rate constant and N_q is the concentration of molecules which contribute to the quenching.

2.2.1 Fluorescence imaging and indocyanine-green for measuring blood flow

Fluorescent molecules, henceforth referred to as *fluorophores* are often used in medical diagnostics for various purposes.[7] They are generally classified as either *endogenous*, which refers to fluorophores that occur naturally in the human body, or *exogenous* referring to fluorophores that do not occur naturally and have to be administered to the patient prior to any diagnostics work.[7] The work in this thesis only concerns work carried out with an exogenous fluorophore. As such, this section primarily focuses on diagnostics with exogenous fluorophores.

Fluorescence imaging is a broad term, which itself can refer to many different types of imaging techniques in which fluorophores are used. In medicine, fluorophores are most commonly used as a type of contrast agent to distinguish between different types of tissue.
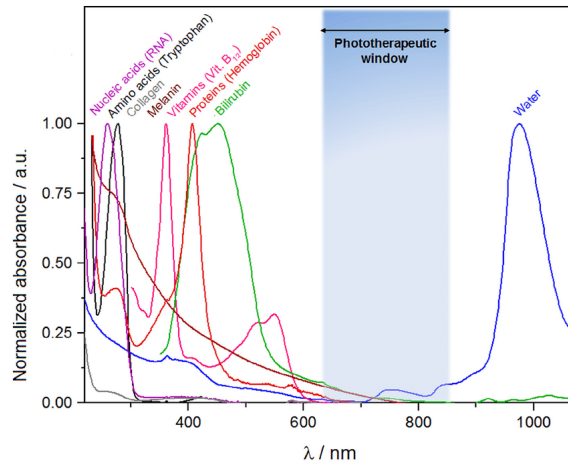
Figure 2.4: The (normalized) absorbance of several common tissue constituents, displaying the therapeutic window where deep light penetration is possible. [8]

There are several imaging techniques which utilize the fluorescence spectrum to deduce medical information. In *fluorescence spectroscopy*, only the wavelength-intensity spectrum is used to characterise the fluorescent signal. Such techniques can for example be used to characterize cancer cells as they display a change in their endogenous fluorescence in comparison to their non-cancerous counterparts. Depending on the imaging depth, it is often beneficial if both the excitation and emission wavelengths are in the so-called *therapeutic window*, where the absorbance of several common tissue constituents is the lowest.

Indocyanine-green (ICG) is a commonly used fluorescent dye which binds to serum albumin, the most abundant protein in human blood plasma.[32] The peak absorbance of ICG is generally observed in the range of 750 to 800 nm, with a fluorescence peak in the near-infrared at approximately 830 nm. This wavelength falls into the aforementioned therapeutic window which leads to easy detection and characterization of the fluorescence signal.
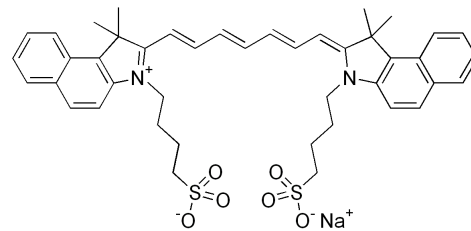
Figure 2.5: The molecular structure of ICG [13] ($C_{43}H_{47}N_2NaO_6S_2$)

Due to its ability to bind to albumin as well as other plasma proteins, ICG is usually used to qualitatively image blood flow.
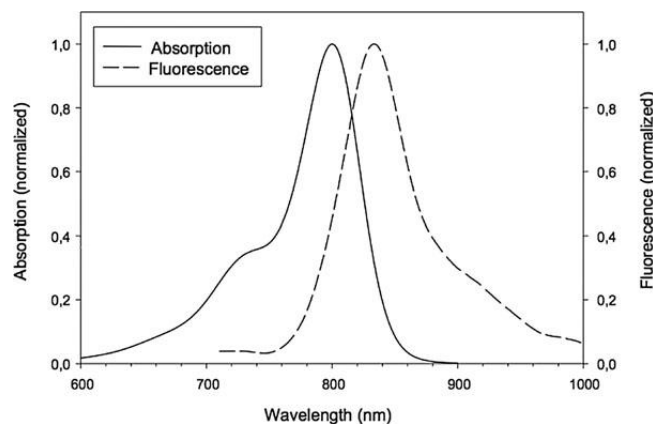
Figure 2.6: Two spectra which indicate the wavelength of the light used for excitation (absorption) as well as the fluorescense signal. [37]

It is hard to make quantitative predictions about for example blood perfusion from the optical image itself,

and one must thus apply some kind of post-measurement analysis to characterize the fluorescence signal.

2.3   Tissue optics

2.3.1   Light-tissue interaction: scattering and absorption

In physics, biological tissues can be described as complex media composed of discrete particles (e.g. cells) that highly scatter and absorb light in an inhomogeneous fashion. [38] Photons will take seemingly random paths and be absorbed or scattered according to the optical properties of the tissue in question. [7]

Due to the complex and seemingly random nature of this process, describing it in a macroscopic and statistical way will prove worthwhile.

The macroscopic attenuation of light in biological tissues is given by the *Beer-Lambert law* [38]

$$I(z) = \left(1 - \frac{(n-1)^2}{(n+1)^2}\right) I_0 e^{-\mu_A z} \tag{2.9}$$

where I_0 is the incoming intensity, n is the average refractive index of the tissue and z is the path length which the light has travelled. μ_A is the *attenuation coefficient* given by

$$\mu_A = \mu_s + \mu_a \tag{2.10}$$

where μ_s and μ_a are the *scattering* and *absorption* coefficients of the medium in question. These describe the average number of scattering and absorption events a photon will undergo per length unit it propagates. Thus, the *mean free path* between two such events is given by

$$l_{fp} = \frac{1}{\mu_A} \tag{2.11}$$

The angular probability distribution for scattering events is given by the *scattering phase function* $\Phi(\hat{\rho} \cdot \hat{\rho}')$, which describes the probability of a photon propagating in a direction $\hat{\rho}$ to be scattered in the incident direction $\hat{\rho}'$. It is normalized such that [7]

$$\int_{4\pi} \Phi(\hat{\rho} \cdot \hat{\rho}') d\Omega = 1 \tag{2.12}$$

Figure 2.7: A depiction of how light is scattered and absorbed in biological tissues, and which paths photons may take in such a medium.

From the scattering phase function, one can define an *anisotropy parameter* as the expectation value of the scattering phase function [7]

$$g = \int_{4\pi} (\hat{\rho} \cdot \hat{\rho}') \Phi(\hat{\rho} \cdot \hat{\rho}') d\Omega = \langle \cos\theta \rangle \tag{2.13}$$

where $\langle \cos\theta \rangle$ is the average value of $\cos\theta$ over all scattering angles θ. For biological tissues, g is usually in the range of $0.8 - 0.98$. [7]

It is worth noting that no general expression of $\Phi(\hat{\rho} \cdot \hat{\rho}')$ exists, and instead, there are several solutions depending on the type of tissue in question. [38] One very common expression that is usually sufficient for

most practical applications is the *Henvey-Greenstein* phase function, given [38]

$$\Phi(\hat{\rho} \cdot \hat{\rho}') = \Phi(\cos(\theta)) = \frac{1 - g^2}{(1 + g^2 - 2g\cos\theta)^{\frac{3}{2}}} \tag{2.14}$$
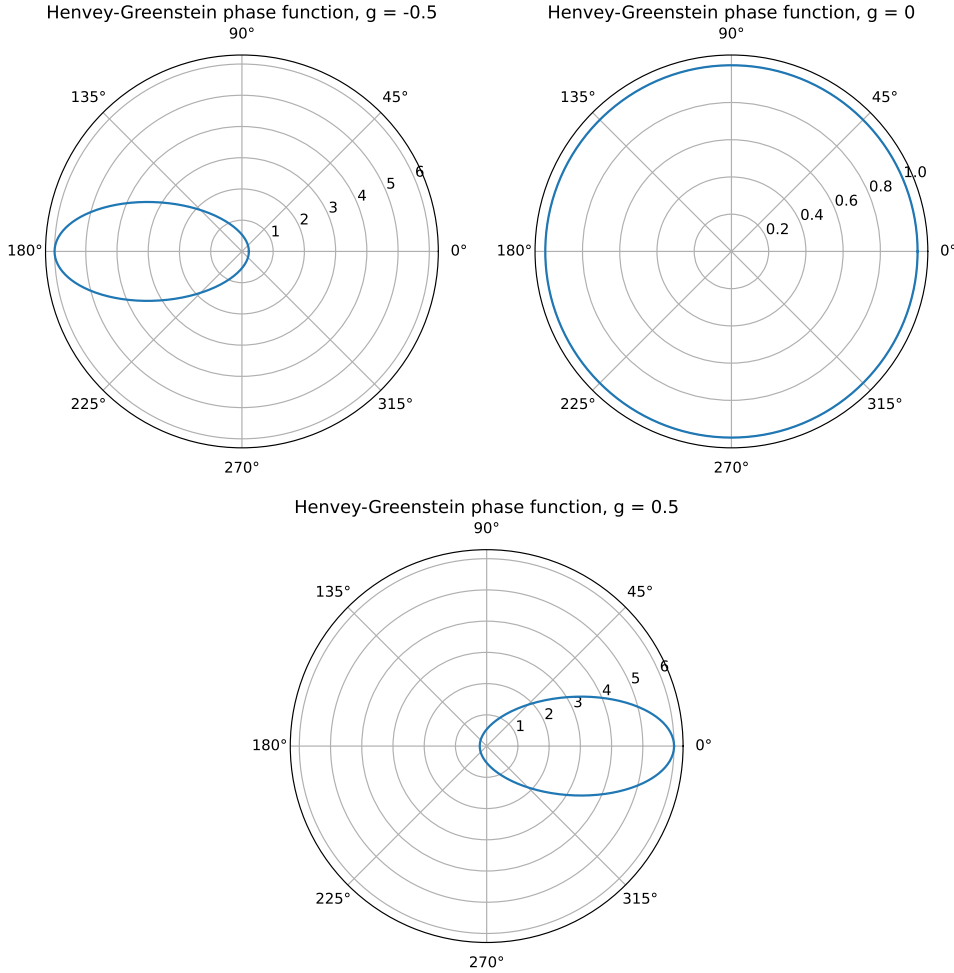
Figure 2.8: Polar plots displaying the Henvey-Greenstein phase function for three different values for g, showing backward, perfectly isotropic and forward scattering respectively. Propagation is taken along the $\theta = 0°$ direction. These all mimic real life cases. $g = 0$ exemplifies how fluorescence would behave for example, whereas the other two mimic a close to coherent light source, such as a laser.

The transport of radiation throughout tissue can be generally described by the *radiative-transfer equation* (RTE). [7] The RTE is a differential equation that describes the transport of power throughout a tissue sample over time, and it takes all energy gains and losses into account.

Let $R(\vec{r}, \hat{\rho}, t)$ denote the *radiance*, which describes the power radiated within a solid-angle element $d\Omega$ through an infinitesimal area element dA. The transport is taken in the $\hat{\rho}$ direction and evaluated at time t and position $\vec{r}$, yielding an expression for $R(\vec{r}, \hat{\rho}, t)$ [7]

$$R(\vec{r}, \hat{\rho}, t) = \frac{dP}{dAd\Omega} \tag{2.15}$$

where dP is the power radiated along the same direction. The RTE for a medium of mean refractive index

n is then given[7]

$$\frac{n}{c}\frac{\partial R(\vec{r}, \hat{\rho}, t)}{\partial t} = \underbrace{-\mu_A R(\vec{r}, \hat{\rho}, t)}_{\substack{\text{Energy loss due to} \\ \text{scattering and absorption}}} \pm \underbrace{\vec{\nabla} \cdot (R(\vec{r}, \hat{\rho}, t)\hat{\rho})}_{\substack{\text{Energy loss/gain due to} \\ \text{divergence/convergence of the beam}}}$$

$$+ \underbrace{\mu_s \int_{4\pi} \Phi(\hat{\rho} \cdot \hat{\rho}')R(\vec{r}, \hat{\rho}', t)d\Omega'}_{\substack{\text{Energy gain due to scattering} \\ \text{of photons into the } \hat{\rho} \text{ direction}}} + \underbrace{S(\vec{r}, \hat{\rho}, t)}_{\substack{\text{Source term, e.g.} \\ \text{a light source}}} \quad (2.16)$$

where c denotes the speed of light in vacuum. The RTE is not soluble analytically unless restricted to simple cases, where it can usually be treated as a diffusion problem. [7] As such, numerical methods such as *Monte-Carlo*-based ones are highly relevant in the field of medical optics.

2.3.2 Monte-Carlo methods for simulating the propagation of light in tissue

Monte-Carlo methods are numerical methods based on generating pseudo-random numbers, repeatedly sampled with respect to a probability density function. When a sufficiently large number of random samples is obtained this can be used to numerically estimate some quantity. [4]

In the C programming language, which is used throughout this project for simulations, pseudo-random number generation is implemented as a recursion relation that yields pseudo-random integers in the range 0 to 32767 [24]

$$\mathcal{R}_{n+1} = \left(\left\lfloor \frac{1103515245 \cdot \mathcal{R}_n + 12345}{65536} \right\rfloor \right) \mod 32768 \quad (2.17)$$

where $\lfloor . \rfloor$ denotes the *floor operation*, equivalent to rounding downwards for positive numbers. It is worth noting that a certain initial value of $\mathcal{R}_n$ (commonly denoted the *seed*) will always yield the same sequence of pseudo-random numbers.

There are several (more or less advanced) Monte Carlo frameworks used to approximate the radiative transfer equation in tissue. One such framework, upon which the simulations performed in this project are based is *MCML* [39], developed by Steven Jaques et al. and published in 1995. There have been several improvements and alterations to this model since, such as the *Multi-Scattering* [28] software package by E. Berrocal and J. Jönsson which runs a voxel-based model on graphics processors. [23]

For the purpose of this chapter, the basic MCML model is sufficient to convey the general simulation steps. The general idea can be viewed in fig. 2.9, and the specifics are described below.

Representation of photons Each model photon is represented by its x, y and z position. To simulate the loss of energy due to scattering and absorption each photon is subsequently given a *weight*, initialized to 1 and then decreased as the photon's energy is attenuated.

If the photon exits the medium, it no longer contributes to the radiance. As such, another variable is added to mark if the photon is still "alive" or if it no longer contributes to the simulation.

In a programming language, this can be done through the use of some composite data structure. For example, in C, one could implement a model photon via the `struct` data type.

```c
typedef struct photon {
    //x, y, z coordinates
    float x;
    float y;
    float z;
    //photon weight
    float w = 1;
    //keep track if the photon
        has exited
    int outside = 0;
} photon;
```

Listing 2.1: An example of an implementation of the model photon described above, as a type-defined standard C struct. The implementation would be analogous in other programming languages

Angles In spherical coordinates both the azimuthal and polar angles need to be taken into account when propagating a photon. The azimuthal angle $\varphi_{i,n}$ at each iteration i for each photon n is given by

$$\varphi_{i,n} = 2\pi \mathcal{R}_{i,n} \tag{2.18}$$

where $\mathcal{R}_{i,n} \in [0,1]$ according to eq. (2.17) (or any other method to generate pseudo-random numbers).

The polar angle $\theta_{i,n}$ is randomly sampled from the *scattering-phase function*. As such all possible values of $\theta_{i,n}$ are not equally likely and the probabilities are given by eq. (2.12). If $\mathcal{R}_{i,n}$ above is once again considered, the weighted random sample of $\theta_{i,n}$ can be obtained by

$$\theta_{i,n} = \mathcal{C}^{-1}(\theta_{i,n})\mathcal{R}_{i,n} \tag{2.19}$$

where

$$\mathcal{C}(\theta_{i,n}) = \int_0^{\theta_{i,n}} \Phi(\hat{\rho} \cdot \hat{\rho}')d\Omega \tag{2.20}$$

Step size The updates to the step size of each photon can be derived from the Beer-Lambert law (eq. (2.9)). The path length at iteration i for photon n is found from

$$l_{i,n} = \frac{\ln(\mathcal{R}_{i,n})}{\mu_A} \tag{2.21}$$

The (x,y,z) coordinate of photon n is then updated by

$$
\begin{aligned}
x_{i+1,n} &= x_{i,n} + l_{i,n}\sin(\theta_{i,n})\cos(\varphi_{i,n}) \\
y_{i+1,n} &= y_{i,n} + l_{i,n}\sin(\theta_{i,n})\sin(\varphi_{i,n}) \\
z_{i+1,n} &= z_{i,n} + l_{i,n}\cos(\theta_{i,n})
\end{aligned} \tag{2.22}
$$

This applies when the photons are sufficiently close to the z-axis, often suitable for tissues as the penetration depth is generally very small.[39] In other cases one instead has to use the so-called *directional cosines* which are also based on spherical coordinates. Exact expressions for these can also be found in the MCML paper[39] by Jaques et. al.

Photon energy loss The energy loss due to absorption and scattering is, as previously mentioned modeled by the weight parameter of each photon. The energy reduction is solely determined by the attenuation coefficient of the tissue in question. As such, the weight at iteration i is updated as

$$W_{i+1,n} = W_{i,n} - \frac{\mu_a}{\mu_A}W_{i,n} \tag{2.23}$$

This accounts for energy losses from both absorption and scattering as μ_A is the total attenuation coefficient taking both the scattering and absorption coefficients into account.

The modifications to this framework to account for fluorescence as well as the specifics related to this project are described further in chapter 4.
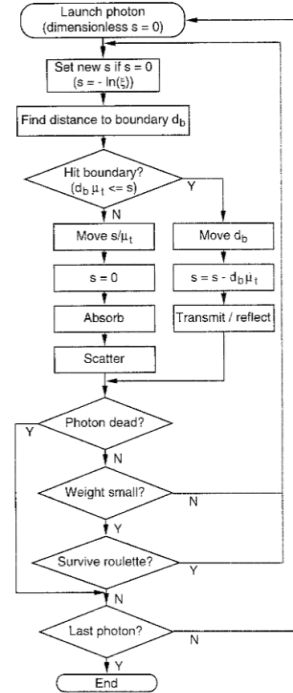
Figure 2.9: A flowchart [39] showing the simulation steps in the MCML framework.

Chapter 3

Medical background

In this chapter, the medical background for this project will be described, starting with a biological description of tissue. After this, surgical treatments for esophageal cancer will be described and finally, the blood perfusion in the area of the anastomosis will be discussed.

3.1 Brief introduction to cells and biological tissue

All living things are composed of *cells*. [3] Even though they are diverse in their size and function, cells share the same basic structure and chemistry. Humans are composed of *eukaryotic cells*, which contain a number of different components (in biology denoted *organelles*). The main distinctor between eukaryotic and prokaryotic cells is that they carry their genetic information, *DNA*, in a structure that is separate from the rest of the organelles (denoted the *nucleus*). [3] Cells are organized into more complex structures by their function, denoted *tissues*. Each type of tissue is also accompanied by *extracellular matrix*, which in various ways supports the function of the tissue.
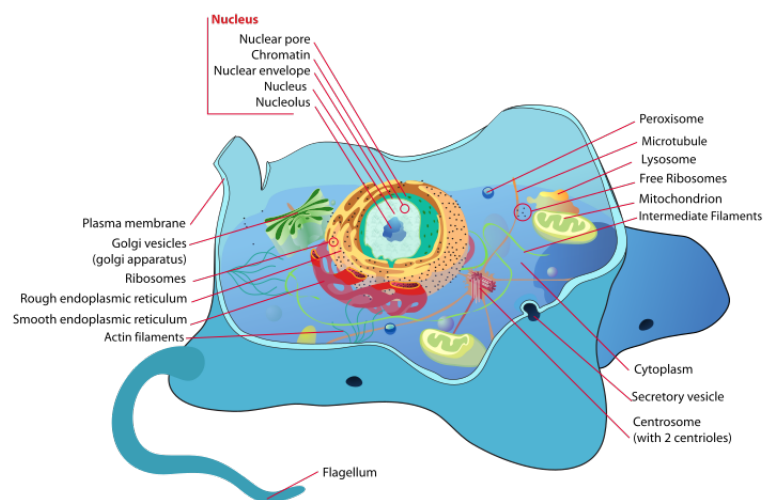
Figure 3.1: The typical structure of an eukaryotic cell, displaying its different constituents. Figure from *Wikimedia Commons*. [42]

A common example is *collagen*, a protein and extracellular matrix often responsible for increasing the tensile strength and rigidity of tissues.[3]

The tissues present in the human body are generally arranged into four main types, namely

1. *Connective tissue*, which binds other types of tissue together.[38] Here, extracellular matrix is usually highly abundant in contrast to other tissue types. Blood is considered a type of connective tissue. [3]

2. *Epitheal tissue* is a protective type of tissue that lines most of the body's organs and cavities.[38]

3. *Muscle tissue*, the main constituent of muscles characterized by its ability to extend and contract on demand.[38]

4. *Nervous tissue* which consists of nerve cells.[38] This is the main component of the nervous system.

3.2   Cancer of the esophagus: anatomy, detection and surgical treatment

3.2.1   Esophageal anatomy

The esophagus is a long and narrow muscular tube which traverses the thorax as well as the upper portion of the abdomen.[9] In an adult it is usually around 25 cm in length and approximately 2 cm in diameter. Its function is to carry food and nutrients to the stomach, where it terminates in a connection to the *cardia*, the uppermost portion of the stomach. The stomach and esophagus are both parts of what is known as the *gastrointestinal system*.[6] The esophageal wall consists mainly of muscle tissue layered with fibrous connective tissue, with an innermost layer of epitheal tissue (*mucosa*).[9]
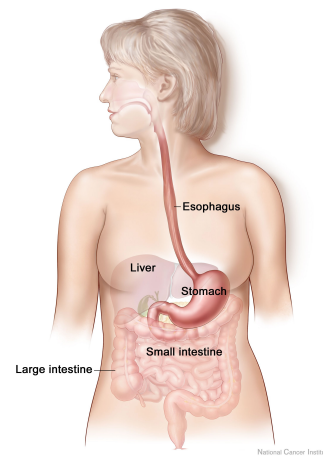
Figure 3.2: An illustration of the gastrointestinal system [12]

3.2.2   Esophageal cancer and its surgical treatment

The main surgical treatment for esophageal cancer is to perform a so-called *esophagectomy* in which parts of or the entirety of the esophagus are resected and subsequently reconstructed.[1] The reconstruction is commonly performed by stretching the stomach, forming a gastric tube which is then surgically attached to the remainder of the esophagus (a procedure commonly known as *esophagectomy with gastric conduit reconstruction*). The surgical connection is medically denoted an *anastomosis*.
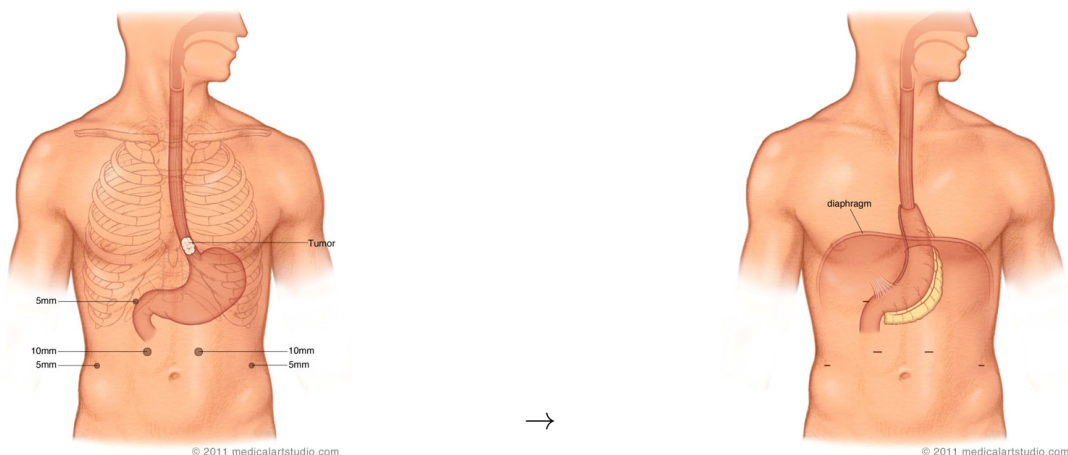
Figure 3.3: Two figures [19] displaying the intestines of the patient before (left) and after (right) having undergone esophagectomy with gastric conduit reconstruction.

There are several complications which may occur, one of the most severe being so-called *anastomotic leak* in which the anastomosis connecting the esophagus and the stomach ruptures. This is a highly severe complication which can lead to multiple organ failure and subsequently, the death of the patient if left untreated.[1] This can occur in all stages of the post-operative process, either due to incorrectly constructing the anastomosis or due to poor healing.

3.3 The cardiovascular system, blood perfusion and its implications for predicting anastomotic leak

3.3.1 Brief anatomic description of the cardiovascular system

Blood is transported throughout the body by *blood vessels*. Vessels through which blood enters the heart are denoted *veins* whereas those that transport blood away from the heart are denoted *arteries*. All oxygenated blood in the body is delivered from the heart and via the *aorta*, a blood superhighway which branches out to different organs in the body.[9] The oxygen is deposited, and the de-oxygenated blood is transferred back to the heart via a network of veins, colloquially the *venus system*. The blood is then once again oxygenated in the lugns, and the cycle repeats. [9]
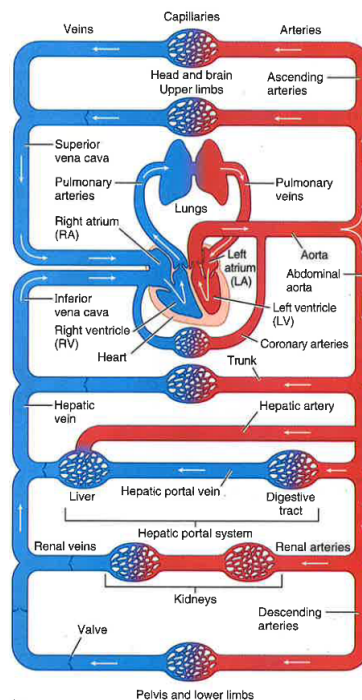
Figure 3.4: A qualitative illustration of the blood flow, or cardiovascular system in a human. Here, red denotes oxygenated blood while blue denotes deoxygenated blood. [9]

3.3.2 Perfusion of the esophagus and stomach

The two main areas of interest in the context of esophagectomy are the perfusion of the esophagus and stomach.

The esophagus is situated next to the thoracic portion of the aorta and is perfused by a group of arteries usually denoted the *esophageal arteries*. These branch from the *inferior thyroid artery*, the *bronchial arter-*

ies, directly from the *thoraic aorta* as well as from an ascending portion of the *left gastric artery*[9] (see section 3.3.2).

When it comes to the stomach, the situation is more complicated: it is perfused by several arteries all branching from the abdominal portion of the aorta. The main artery of interest for the purpose of this report is the *gastroepiploic artery* which runs along the greater curvature of the stomach, as most of the other vascular sources are removed as part of the esophagectomy procedure. This artery is itself a branch of the *gastroduodenal artery* which in turn branches from the *hepatic artery*. As such, the delivery of blood to the stomach through the gastroepiploic artery is not as direct as for the esophagus, as blood has to travel through several branching arteries before reaching it.
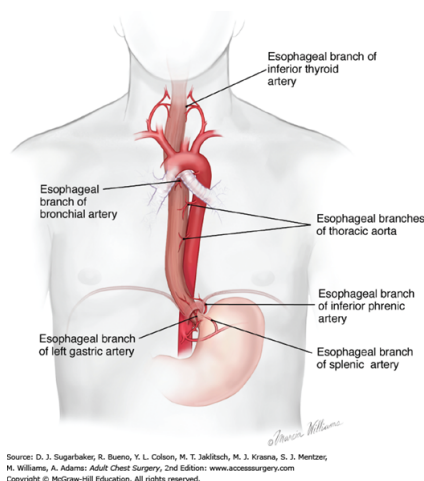
Figure 3.5: The esophageal blood supply. Here, it is highly visible that it is close to directly supplied by the aorta. [35]
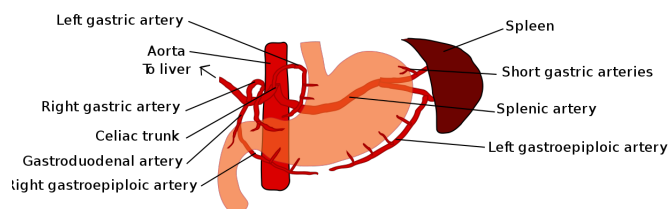
Figure 3.6: Illustration showing the arterial supply to the stomach, where one can see the complicated network leading to a high degree of vascularization. [27]

3.3.3   Arterial supply to the anastomotic area, post esophagectomy

The area above the anastomosis, i.e. the remainder of the esophagus is still well perfused by its near direct connections to the thoracic aorta post esophagectomy. The area below the anastomosis, i.e. the gastric conduit constructed from the stomach is supplied solely via the gastroepiploic artery. One can expect a gradient to arise in the blood pressure along the direction of the stomach, with the perfusion being the highest in the lowest point of the gastric conduit and consistently decreasing upwards. As such, the area directly below the anastomosis will always be poorly perfused in contrast to the area above it. Furthermore, it is highly sensitive to physiological stress. The gastroepiploic artery is a part of the splenic circulation. This is not a vascularly prioritized circulation in these conditions as it contains many organs that are not as vitally essential (such as the spleen). The conclusion is that due to the vulnerable nature of the anastomosis, there is a major risk for the patient to develop leakages. If any discrepancies in the perfusion should arise, the already poor perfusion of the stomach will be further affected. This could in turn lead to worsened and slower healing of the anastomotic area.
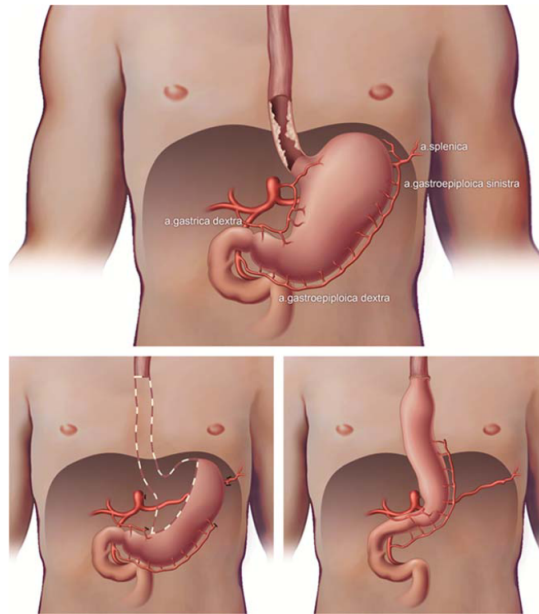
Figure 3.7: The blood supply to the gastric conduit post esophagectomy. [20]

Chapter 4

Simulating ICG fluorescence with Monte-Carlo techniques

As this work encompasses image analysis work to a large degree, Monte-Carlo simulation techniques have been used to predict the light distribution from ICG fluorescence in the esophagus. These simulations have subsequently been used as a basis for the development of the image-analysis software, and also serve a qualitative purpose. The simulation software subsequently generates a video file, in which the expected progression of the fluorescence image is shown.

To account for the possibility of an anastomotic defect as well as fluorescence, a new software package has been developed specifically for this purpose, based on the aforementioned MCML package by Jaques. et. al. [39]

In this chapter, the methods and assumptions of these simulations, are presented.

4.1 The ICG-sim software package

4.1.1 Implementation

ICG-sim is implemented in the C17 (ISO/IEC 9899:2018) [18] standard of the C programming language [24], and uses the OpenMP API[29] for parallelization to make execution more efficient. The complete source code can be found at the end of this thesis, or accessed at https://github.com/lkildetoft/ICG-sim.

Number of photons	Number of iterations	Runtime (OpenMP enabled)	Runtime (OpenMP disabled)
$1 \cdot 10^6$	500	≈ 5.53 s	≈ 26.8 s
$1 \cdot 10^7$	500	≈ 32.3 s	≈ 2 m 14 s
$1 \cdot 10^8$	500	≈ 5 m 36 s	≈ 22 m 29 s

Table 4.1: Benchmark of one run of the ICG-sim software package, with and without OpenMP parallelization enabled and with a different number of photons for each run. All of these simulations had identical parameters otherwise and were run on an Intel Core i5-4590s quad-core CPU[17] with 24 GB of DDR3 ram.

The software package can be considered a derivative of the original MCML software[39] as it uses the same basic routines (although implemented from scratch) for photon propagation, but with a geometry which specifically mimics a tissue slab of the gastric conduit after esophagectomy. It also includes extensions to

account for fluorescence as well as the gradual uptake of ICG when injected into the human circulatory system. These extensions are further explained in sections 4.1.2 and 4.1.3 below respectively.

4.1.2 Simulating an incoherent light source

Generally, illuminating as much of the area of interest as possible is beneficial, as this allows fluorescence to be induced in more points than if one utilizes a coherent light source (e.g. a laser).

In the subsequent instrument, an optical fibre will be used as for light delivery. When photons exit the fiber tip they will generally acquire a large angular divergence. This leads to a conical beam profile as shown in fig. 4.1.
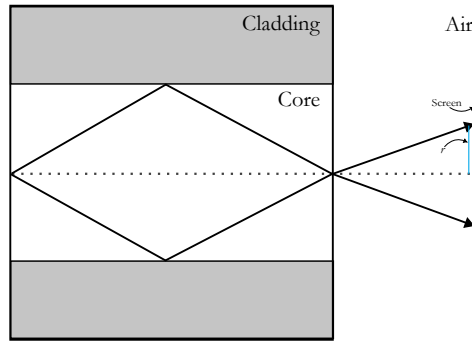
Figure 4.1: A qualitative illustration of light rays exiting an optical fiber, showing the conical divergence as discussed above.

In ICG-sim the fiber tip is assumed to behave as a point source with coordinate $(x, y, z)_{source}$. Each photon is then given the starting coordinate

$$(x, y, z)_{n,start} = (x, y, z)_{source} + (r_n \cos \varphi_n, \; 0, \; r_n \sin \varphi_n) \tag{4.1}$$

where r_n is a random number between 0 and r (see fig. 4.1) and φ_n is also a random number but this time between 0 and 2π. This distributes the photons such that they all lie within a circle of radius r on the outermost surface of the simulation geometry.

4.1.3 Accounting for gradual ICG uptake and anastomotic defect

When ICG is injected into the human bloodstream, it will gradually be delivered to the esophagus at a speed proportional to the blood perfusion. This gradual uptake continues until it reaches the injected concentration.

In ICG-sim, each photon can either interact with respect to the attenuation coefficient of the tissue or the attenuation coefficient of ICG. The frequency of these interactions is governed by the probability of encountering ICG at each iteration, which can be considered proportional to the concentration of ICG at each time following injection. In ICG-sim, this probability grows at a fixed rate at each iteration until it reaches a maximum value, after which it is kept constant.

To account for anastomotic insufficiency, the simulation geometry has been divided into three distinct parts in which the ICG concentration can grow at different rates. These rectangular areas cover the entire slab in the $x-$ and y directions and are solely defined by their z positions.

As is described in Chapter 3, a pressure gradient will arise along the gastroepiploic artery, which is decreasing with the positive z-direction in fig. 5.3. This leads to a slower perfusion speed directly below the staple

row than at the bottom of the simulation geometry. To simulate this gradient in the perfusion speed the ICG concentration in this region is updated according to (where z_{max} is the z position of the anastomosis)

$$c_{i+1}(z) = c_i(z) + \kappa_{max} \left(1 - \frac{\kappa_{grad} \cdot z}{z_{max}} \right) \quad (4.2)$$

where κ_{max} is the concentration update rate at $z = 0$ and $0 \leq \kappa_{grad} \leq 1$ is the fraction of κ_{max} at which the blood pressure decreases with each step in z.

The light source in the final instrument will be continuous and illuminate the region of interest during the entire data-taking process. To simulate this continuity, photons are launched from their starting positions in packets given by the total number of photons divided by the total number of iterations. At each iteration, both all previously launched photons as well as a new packet are propagated. This continues until the last iteration, where all photons are subsequently propagated.
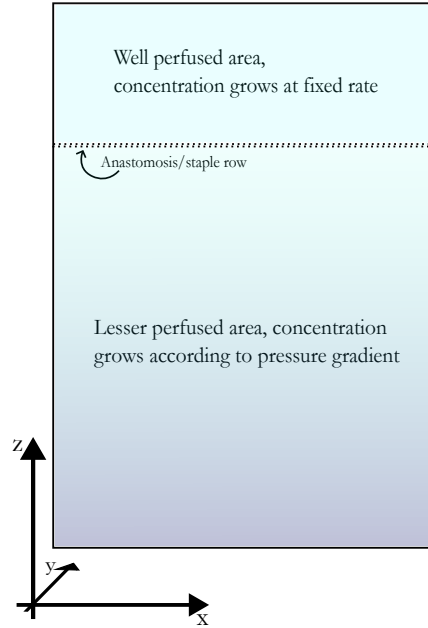
Figure 4.2: A 2d representation of the simulation geometry, with the three rectangular regions indicated. In actuallity, the simulation also considers a depth, indicated by the y-axis in the figure. Illumination is done in this direction as well.

4.1.4 Accounting for fluorescence

When a photon encounters ICG and its weight is below a pre-set threshold, a fluorescence event can be induced in proportion to a pre-defined probability. The existence of a finite probability for fluorescence can be considered as an analog for quenching, as described in section 2.1.2.

If a fluorescence event is induced, it will re-launch the photon but it will now be pre-conditioned to instead interact according to the optical parameters for the fluorescence wavelength. If a fluorescence photon reaches a distance of 1 mm to the front face of the simulation slab, it is considered to be detected and the subsequent distribution of fluorescence photons is saved. The re-use of pre-existing photons instead of launching new fluorescence photons is mainly motivated by its memory efficiency, and should not lead to any discrepancies in the physical accuracy of the simulation as only the detection of fluorescence photons is considered in the resulting histograms.

4.1.5 Limitations

As aforementioned, directional cosines are not used and all interactions are assumed to take place close to the z-axis. This may provide inaccuracies in the resultant photon distribution if detected over large distances, but for verification purposes, it is safe to assume that the detection of the photons takes place sufficiently close to the z-axis. In an endoscopy situation, the endoscope will surely always be located close to the anastomosis with a separation on the order of a few centimeters.

Even though the simulation is based on an experimentally verified previous model by Jaques et. al. there may be errors in the representation of the fluorescence signal. Furthermore, it is not known if the expected pressure gradient in the patient's blood flow is completely linear, even though it seems like a physically sound assumption. This is of course a big limitation of this model.

This is however not at all the main focus of this thesis. The Monte-Carlo model is only used for verification purposes, mainly for the image analysis software. As long as the model provides a gradually increasing probability for photons to interact across the simulation geometry, it should be enough to verify that the image analysis algorithm can characterize deficiencies. Any added level of physical accuracy is merely a bonus in this case.

Chapter 5

Quantifying ICG fluorescence: an algorithmic approach

As aforementioned, the presence of a fluorescence signal itself is not the main factor of interest to determine if the blood perfusion in the anastomotic area is poor. As long as ICG is delivered, it can be expected to fluoresce at some point.

In this chapter, methods to quantify ICG-fluorescence in a perfusion based setting are discussed. Firstly, a current state of the art is provided. Then, two algorithms which were developed specifically for this thesis are discussed, and verified using Monte-Carlo simulations. Lastly, time evolution measurements on tissue phantoms that crudely mimic blood perfusion are presented.

5.1   State of the art

Nerup. et. al. have previously presented a software algorithm for real time perfusion assesment utilizing ICG, which performs very well. This algorithm (*Q-ICG*) utilizes a similar type of metric as the ones presented here, namely an estimation of the fluorescence time-intensity slope. This is done by performing a linear regression on the recorded fluorescence signal with respect to a baseline. Several studies have been performed where *Q-ICG* is utilized to monitor perfusion speed. The main take-away is that utilizing the time-intensity slope is a very reliable way of analyzing these types of measurements.

The second algorithm presented here provides what can be viewed as an alternative approach to calculating the same metric as *Q-ICG* does. Here, a numerical approximation of the derivative is used in lieu of linear regression. Further, this is tested against another algorithm which instead utilizes the absolute time to fluorescence maximum, which is meant to be used in conjunction with the second if this proves worthwile. As such, the work presented here can be seen somewhat as a unique extension to *Q-ICG*.

5.2   Two metrics for time-evolution measurements

When imaging the anastomotic region, we can assume that each pixel will experience a maximum intensity $I_{max,i}$ where i denotes the pixel number. Let the intensity evolution for each pixel be given by $I_i(t)$. To

approximate this function, the pixel value needs to be sampled over time such that a sequence of values

$$I_\Omega = \{I_i(t_n) \mid t_n \in \mathbb{R},\ t_0 \le t_n \le t_{max}\}$$

for each pixel is obtained. If this is the case, two metrics are of interest to estimate the blood perfusion in the area:

1. The time it takes for pixel i to reach a certain threshold fluorescence intensity I_{fluor}, e.g. solve $I_i(t_n) = I_{fluor}$ for t_n, to compute $\Delta t = t_n - t_0$.

2. An approximation of the time derivative $\frac{\partial}{\partial t}I_i(t)$, e.g. the slope of the fluorescence intensity curve per pixel.

A slow evolution of the pixel intensity would, in turn, be suggested by a large time difference $\Delta t = t_n - t_0$ and a small time derivative in contrast to the surrounding pixels.

In the case of this thesis project, both metrics are used and evaluated. The first metric would likely suffice in many cases, but has a big disadvantage: one may, depending on the measurement conditions, need to establish a threshold intensity (I_{max}) which may vary in different conditions. One can however utilize the maximum intensity per pixel. The second metric however completely avoids this, as it is independent of any case-to-case differences in I_{max}.

As it is not inherently clear if $I_i(t)$ is linear in time, the derivative has to be approximated numerically. The following symmetric difference formula has been shown to provide accurate enough results in terms of its truncation error.[31] Given a step size t_{step}, we approximate $\frac{\partial}{\partial t}I_i(t)$ as

$$\left.\frac{\partial}{\partial t}I_i(t)\right|_{t=t_n} \approx \left.\frac{I(t+t_{step}) - I(t-t_{step})}{2t_{step}}\right|_{t=t_n} = \frac{I(t_{n+1}) - I(t_{n-1})}{t_{n+1} - t_{n-1}} \tag{5.1}$$

To form a qualitative and human-understandable picture of where in the imaged region the ICG concentration is growing slowly, a mapping is used where each pixel is assigned an RGB value (a so-called colormap) depending on the value of $\frac{\partial}{\partial t}I_i(t)$. If a distinct region of pixels in which $\frac{\partial}{\partial t}I_i(t)$ is significantly small, this is marked as a *danger zone* in which the blood flow in the tissue is poor and may require surgical intervention.

Two algorithms were developed, utilizing each metric. These are described in the following two sections. To evaluate if they properly provide a picture of how intensity signals evolve over time, and if they are appropriate for ICG-fluorescence, they were first evaluated on Monte-Carlo simulations as well as on tissue phantoms.

Both algorithms are designed so that they carry out the calculation of each of the above metrics frame-by-frame and pixel-by-pixel. They both utilize this to generate a colormapped image of the fluorescence evolution in each pixel. This image has the same dimensions as a single frame.

5.2.1   Algorithm I: absolute time

The pseudo-code below (algorithm 1) provides a basic implementation template for the absolute time algorithm.

Algorithm 1: Absolute time

Input: Array of frames $F_{k \times m \times n}$, threshold intensity T, framerate s
Output: Matrix $M_{m \times n}$
begin
    $n \leftarrow 0$
    for $p \leftarrow 0$ **to** k **do**
        $f \leftarrow F[p]$
        for $i \leftarrow 0$ **to** m **do**
            for $j \leftarrow 0$ **to** n **do**
                if $(f[i,j] \geq T) \wedge (M[i,j] = 0)$ **then**
                    $M[i,j] \leftarrow n/s$
                else
                    $M[i,j] \leftarrow 0$
                end if
            end for
        end for
        $n \leftarrow n + 1$
    end for
end

This implementation may in certain programming languages provide a poor time complexity due to the triple for-loops. As such, in the Python implementation used in this thesis, several optimizations have been made using the *numpy* package [31]. The full analysis code can be viewed in Appendix B of this report.

5.2.2 Algorithm II: fluorescence slope

Here, a pseudo-code template for implementing the fluorescence slope metric as is done in this thesis is provided.

Algorithm 2: Fluorescence slope

Input: Array of frames $F_{k \times m \times n}$, framerate s
Output: Matrix $M_{m \times n}$
begin
    for $p \leftarrow 1$ **to** $k - 1$ **do**
        $f_1 \leftarrow F[p-1]$
        $f_2 \leftarrow F[p+1]$
        for $i \leftarrow 0$ **to** m **do**
            for $j \leftarrow 0$ **to** n **do**
                $M[i,j] \leftarrow M[i,j] + \frac{f_2[i,j] - f_1[i,j]}{2*(1/s)}$
            end for
        end for
    end for
    $M \leftarrow M/k$
end

The same specifities regarding the time-complexity as in the previous section once again apply.

5.2.3 Verification using Monte-Carlo simulations

A single Monte-Carlo simulation was performed for verification purposes.

Optical depth	5 cm
Size of slab	2 x 2 x 5 cm
Esophagus scattering coeff.[38]	29.5 cm^{-1}
Esophagus absorption coeff.[38]	3.3 cm^{-1}
Injected ICG concentration	0.25
Anastomosis location	Pixel row 420

Table 5.1: The parameters used for the Monte-Carlo simulation.

The obtained figures for this simulation with the optical parameters in table 5.1 can be viewed below.
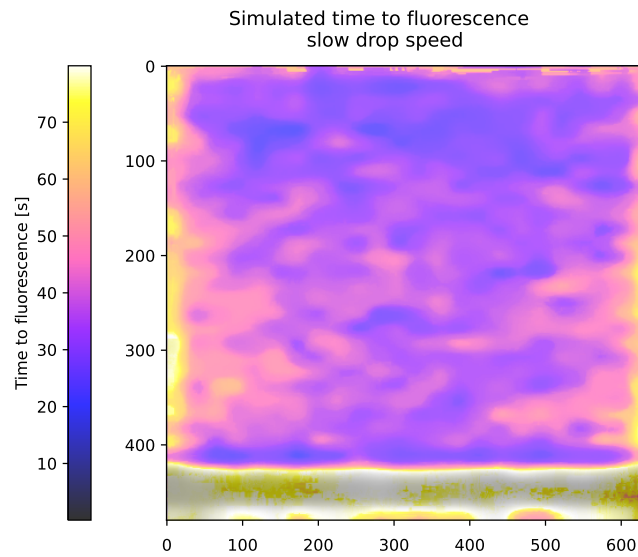
Figure 5.1: The absolute time algorithm applied on the aforementioned simulation
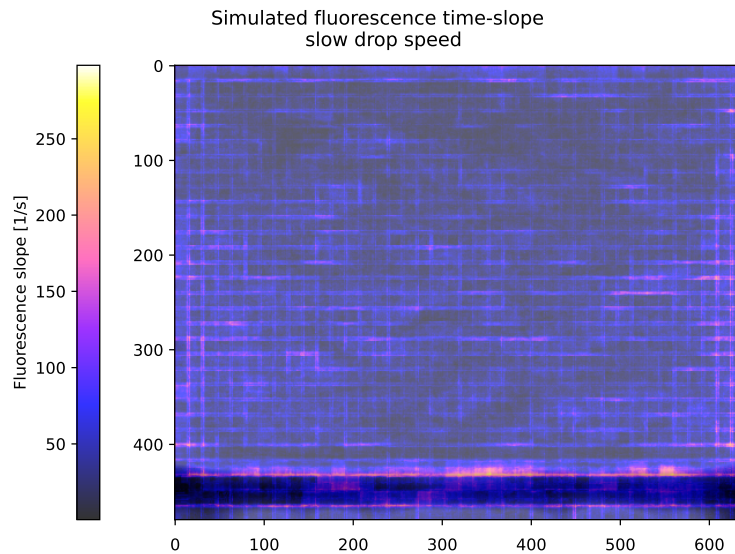
Figure 5.2: The fluorescence slope algorithm applied on the same simulation as in fig. 5.1.

24

Both of these figures do display the time evolution throughout the simulation geometry. The absolute time algorithm clearly shows the trend, whereas it is a bit more unclear in the fluorescence slope figure. These tests do however fulfill their purpose of verifying if the algorithms can detect trends in the time-evolution in conditions similar to the expected tissue conditions.

5.3 Time evolution measurements of ICG-fluorescence in tissue phantoms

Several experiments were performed where ICG fluorescence was measured in tissue phantoms. The main purpose of these were to test the two image analysis algorithms for different cases, especially different time evolutions. It is not inherently known what the perfusion speed in a subsequent patient may be, and it is likely that it varies from patient to patient, if they have a medical history of arterial pressure disease, for example. It is of interest to know if each algorithm performs better for a certain case, and if it is beneficial to use both for providing a complete picture of the blood perfusion in the anastomotic region.

5.3.1 Experimental setup and methodology

The main plasma protein in blood to which ICG binds is as aforementioned *albumin*. Albumin (human) solution is readily available for clinical use in varying concentrations.

The tissue phantoms designed for this experiment are albumin solution, at a concentration of 50 g/l (which mimics arterial conditions) mixed with an aqueous ICG solution. The subsequent concentration is the same as is used in most clinical circumstances, at roughly 5 mg/ml.

The solution is hosted in a plastic cuvette with a thickness of 3 mm. This is on the same order as the esophageal tissue and mucosa which the laser has to penetrate. As such, it provides a good compromise in place of actual, perfused tissue to study ICG-fluorescence.

Figure 5.3: Tissue phantom solution which is used in this thesis.

A picture of the setup used in these experiments can be seen below in fig. 5.4.

The light source used is a 760 nm DFB laser diode (*Eagleyard photonics DFB-0760-00040-BFW01-0002*) coupled into a single-mode optical fiber.
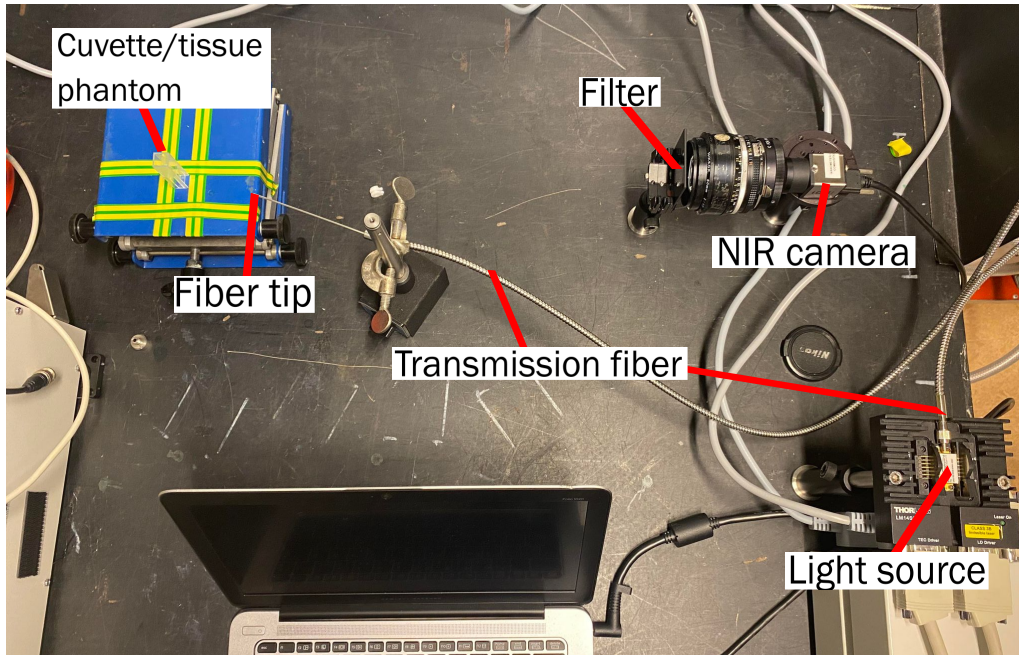
Figure 5.4: A picture of the experimental setup used in the tissue phantom measurements, indicating the different components.

The fluorescence image is obtained utilizing a near-infrared enhanced CMOS camera, which is highly sensitive to light in the $\sim$780 nm to 2.5 μm wavelength region (*IDS Imaging UI-5240CP-NIR*). The incident light is filtered before impinging on the camera sensor, something which is highly necessary: the fluorescence signal may be quite low, and as the camera images monochromatically it would therefore be indistinguishable from background light and reflections. The filter used is a *Schott RG830* longpass-filter which has a steep transmittance cutoff below 830 nm.

The experiment is based on successively filling the empty plastic cuvette with tissue phantom while illuminating it and simultaneously recording it with the camera. The Monte-Carlo simulations have a already verified that the algorithms indeed can distinguish differences in the time evolution over the imaged region. As such, two measurements were performed here: one where the cuvette was filled very quickly, and one where ICG-albumin was instead slowly added.

With the camera and light source aligned and turned on/recording, tissue phantom was added to the cuvette with a plastic pipette. In the fast case, it was quickly ejected with a single squeeze whereas for the slow case, it was dripped with constant speed over a duration of 54 seconds.

5.3.2   Results - slow drop speed
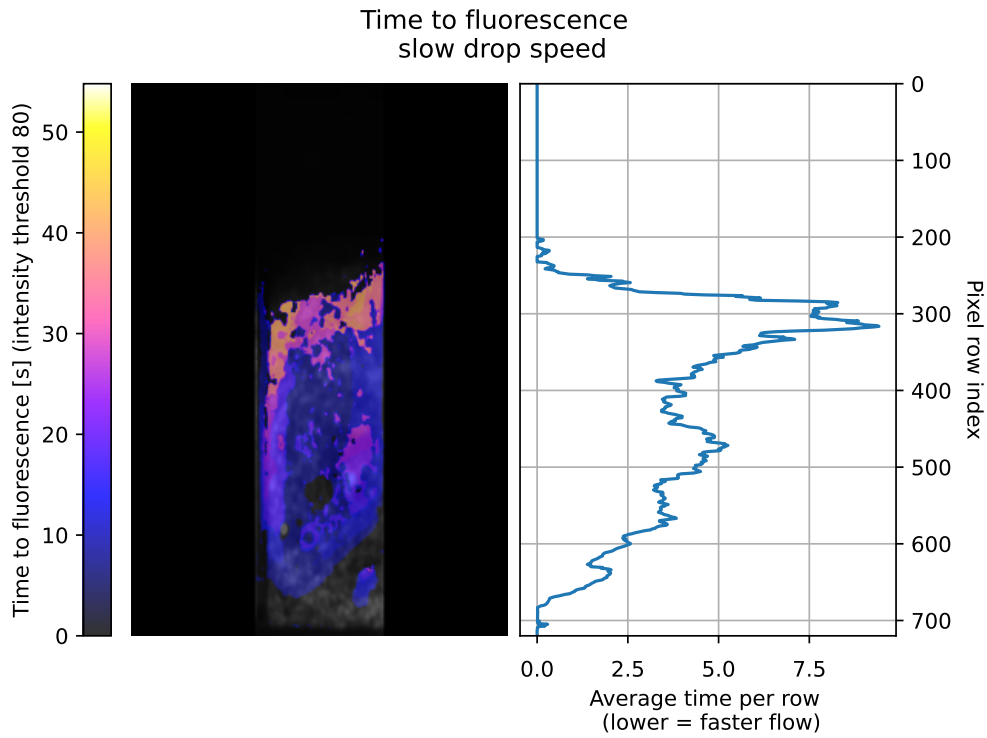
Figure 5.5: The absolute time algorithm applied on a slow drop speed measurement. Here, tissue phantom was slowly added to a cuvette over 54 seconds while illuminated and imaged. The rightmost plot displays the time per row of pixels of the final image, to further indicate if there are any discrepancies in the time to fluorescence is reached.
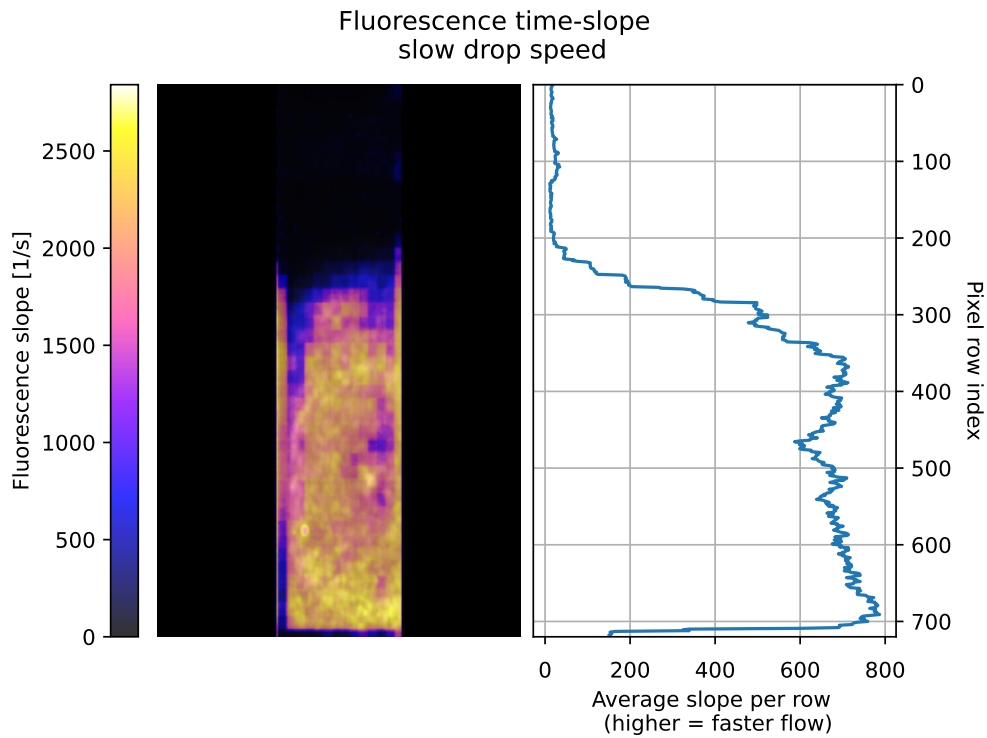
Figure 5.6: The fluorescence slope algorithm applied on the same measurement as in fig. 5.5.

5.3.3 Results - fast drop speed
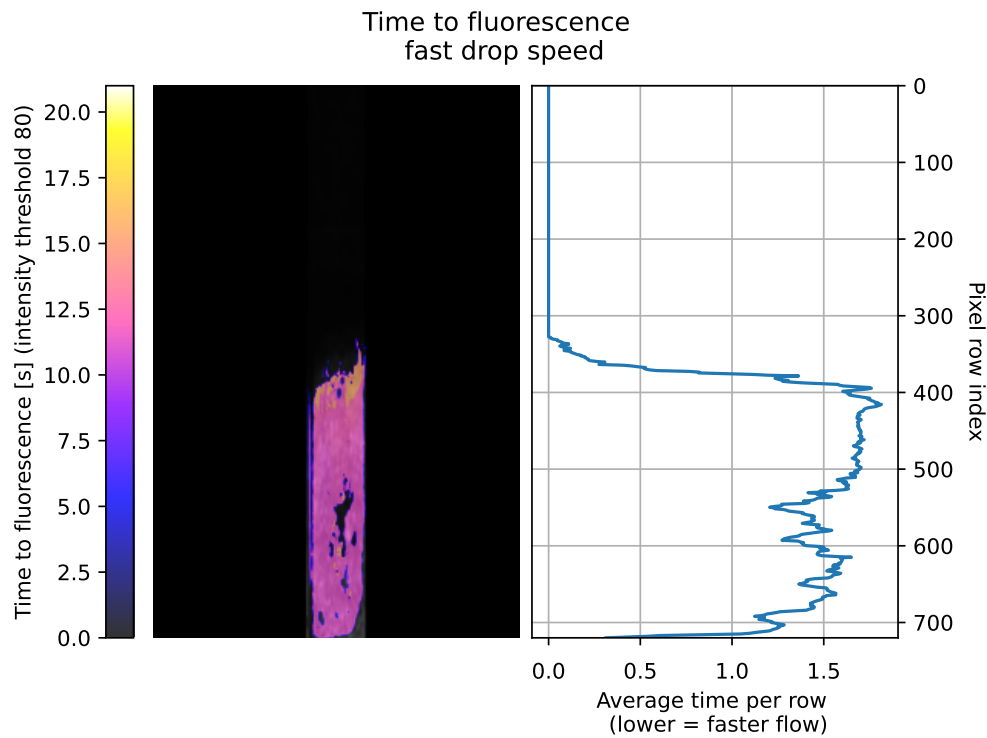
Figure 5.7: The absolute time algorithm applied on a measurement where ICG was quickly ejected into the cuvette. Once again, the average time per row of pixels is plotted to further display any discrepancies which are not visible from the colorbar on its own.
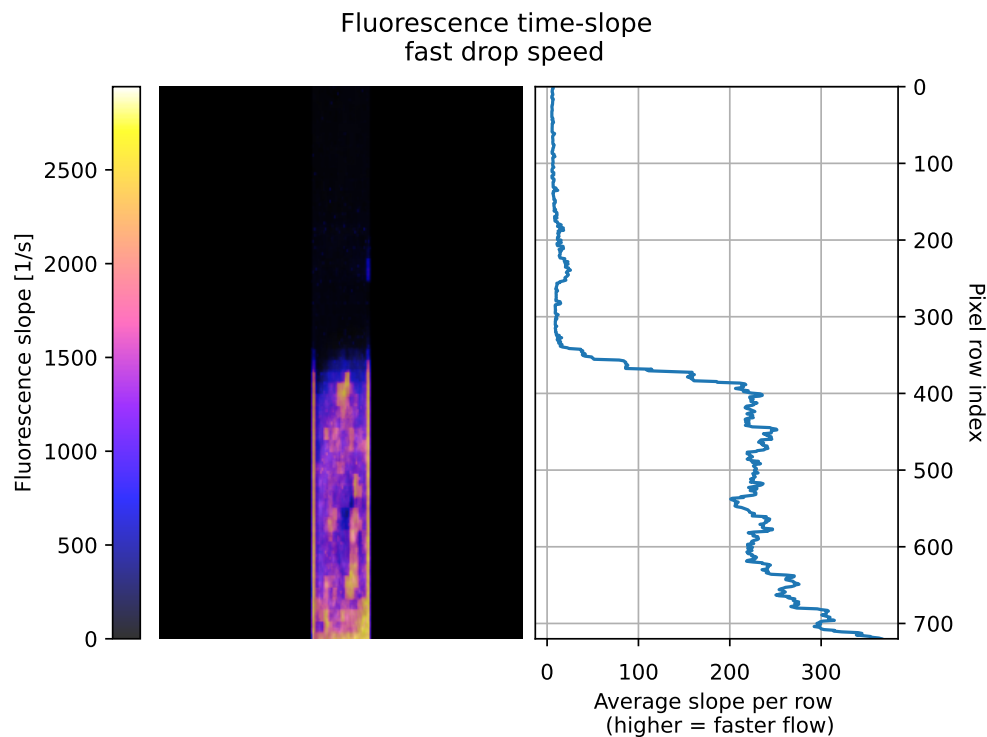
Figure 5.8: The fluorescence slope algorithm applied to the same measurement as in fig. 5.7

5.3.4 Discussion

From the drop speed measurements above, it is clearly indicated that the two algorithms in both cases provide a quantitative picture of how the fluorescence signal evolved throughout the imaged region. This can be seen for both cases from the average row-time graph on the right in each figure: there are clear differences across the geometry in both cases. As the cuvette was filled down and upward by dripping, it was mainly interesting to look at the average values of the pixel rows. This may not be the case in actual measurements however as discrepancies may also arise along the width of the image. As such, it may be of great interest to look at the pixel-column averages in conjunction with row averages in measurements where this is relevant.

If comparing fig. 5.5 and fig. 5.6 (i.e. absolute time and fluorescence slope for the slow drop case) purely from the color-mapping, it is seen that fig. 5.5 provides a much clearer picture of the evolution of the fluorescence signal. This is highly reasonable from a mathematical standpoint: if the time difference between each droplet entering the cuvette is small enough the drop speed will be close to constant. The drop speed is proportional, or even identical to the time-intensity slope. There is however a large difference between the maximum time (top of the cuvette) to fluorescence and the smallest, leading to it being distinguishable in the absolute time case.

The contrary is true for the fast evolution case. Here, the difference between the maximum and minimum times is too small to be visualized, and one as such obtains a close to homogenous color-mapping. The fluorescence slope algorithm however manages to provide both an understandable and quantitative picture of the time evolution throughout the geometry.

In a clinical setting, the algorithm needs to be able to detect vanishingly small discrepancies in the blood flow of the patient. It is not inherently known if one will obtain results similar to the slow drop or fast drop measurements, and this may even differ throughout the imaged tissue. As such, it could be reasonable to combine the two algorithms to form a complete picture: in regions of the tissue where the difference between the maximum and minimum time is large, the absolute time algorithm could be used. Similarly, the fluorescence slope algorithm could be used in regions where the contrary applies. By combining all imaged regions into one image, one would be able to obtain a full picture of the tissue perfusion while alleviating the difficulties with each algorithm.

Chapter 6

In vivo measurements to predict anastomotic insufficiency in a porcine model

This chapter presents results obtained over two days from studies performed at Umeå University Hospital (*Norrlands universitetssjukhus*). These were performed *in vivo* in a pig, where the small intestine was used as a model for the esophagus as well as the ventricular tube. These results serve as a proof-of-concept of how the technique could be applied in humans as the tissue conditions can be expected to be highly similar. The studies were all performed in conjunction with all animal ethics regulations (*etikansökan A-32-19*), with doctors who had all undergone ethics training specific to pigs.

6.1 Surgical and experimental procedure

The measurements were performed on a healthy, adult pig that had been raised and cared for at a nearby farm. After having been anesthetized, a portion of the small intestine was extracted through an incision in the abdomen. Three separate anastomoses were sewn, although only two of these were used for the final measurements. One part of each was left unaltered, retaining its previous vascularization. This mimics the direct aortic blood supply in the human esophagus. The other part had a certain number of arteries limited in their perfusion speed, utilizing surgical clips. Two of the anastomoses were clipped so that they retained a one-to-three de-vascularization ratio (i.e. one of three arteries was clipped), and the third one with a two-to-three ratio. This subsequently mimics the poor blood supply in the ventricular tube.

The ICG was mixed with distilled water to the typical clinical concentration of 5 mg/ml, and injected followed by flushing with saline. The pig had an allergic reaction immediately following both injections, but anaphylaxis was quckly avoided by adrenalin treatment. The injections were performed through an artery in the right frontal leg of the pig.
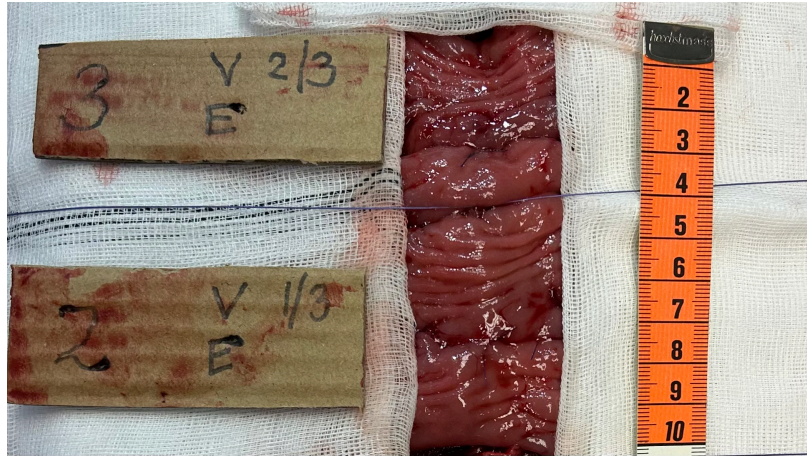
Figure 6.1: The two imaged anastomoses, with de-vascularization ratio indicated to the left. The anastomoses are located at roughly 2.6 cm and 7.3 cm respectively, according to the ruler to the right. This can be seen from the visible stitches. The part above this line in each is the de-vascularized part.

Imaging was done from above, with a ceiling-mounted NIR camera with *Schott RG830* longpass filter. The camera used was once again the *IDS Imaging UI-5240CP-NIR* as in the previous chapter. Two of the three anastomoses were illuminated using the 760 nm DFB laser diode (*Eagleyard photonics DFB-0760-00040-BFW01-0002)* coupled into a single-mode optical fiber as in the previous chapter. The reason for only illuminating two anastomoses was a compromise due to the power loss of the light source being too great at the distance required to illuminate all three: it was unclear if one would be able to achieve fluorescence at all. As such, it was set at a distance where a fluorescence signal could be verified using a phantom containing diluted ICG, and the two-to-three ratio as well as one of the one-to-three ratio anastomoses were illuminated and subsequently imaged.

Two ICG injections were performed, with 30 minutes of downtime between each to allow the chemical to saturate and be cleared hepatically. The two anastomoses were simultaneously recorded during the full course of ICG circulation until saturation appeared to have been achieved.

After the full procedure, the pig was sacrificed per standard regulations.

6.2 Data processing

The videos were processed with the aforementioned scripts, also used in the previous chapter (see Appendix B for the implementation). In addition to this, standard deviations for each pixel were also calculated and visualized.

The standard deviation for a single pixel value x is defined as

$$\sigma = \sqrt{\frac{(x - \mu)^2}{N}} \tag{6.1}$$

where μ is an arithmetic mean extracted from the data containing x, and N is the total number of pixels. The standard deviation is a commonly used statistical measure that is interesting to investigate in the case of this project. It may further reveal discrepancies in the produced figures, especially when correlating between the two.

In the case of figures produced using algorithm 2, the average derivative in the same well-perfused area of the image was used in place of μ. For algorithm 1, a mean time to saturation in a well-perfused region over all four images was calculated and used as μ. The reasoning behind using μ-values obtained only in well-perfused regions of the tissue is that it is more physiologically relevant than utilizing the mean value over

the full fluorescence image. Doctors are interested in knowing how much a certain region of tissue deviates from what is considered a physiological standard for well-perfused tissue, rather than from a mean value that might be biased by the regions that performed poorly. The value for I_{fluor} used in the absolute time measurements was the saturation intensity for each pixel. This provides a slight modification according to the previous chapter, where a common threshold was used for all pixels. In a physiological context this is reasonable: one cannot agree on a physiological maximal saturation intensity as this could vary greatly from patient to patient. Furthermore, the light source, injected ICG concentration as well as the camera used would all affect this as well. The algorithm should be general, and as such the intensity of each pixel in the last frame of the sequence is used as the threshold.

The colormappings were also normalized in contrast to the previous section, to avoid the confusion which may arise from a low slope not indicating the same as a short time, rather the opposite. A different colormapping is used in these figures, which provides more steps to display small differences. Furthermore, the ranges were set such that red tones indicate poor perfusion for both algorithms, whereas blue indicates good.

6.3   Results, injection 1

As aforementioned, two separate ICG injections were performed and the same two anastomoses were imaged. This resulted in four separate recordings, which in turn resulted in a mean time to saturation of 29 seconds in a well perfused area, as well as a slope of 600 s^{-1} being considered the lower limit for poor perfusion, and 1000 s^{-1} the opposite.

6.3.1   Anastomosis 1, de-vascularization ratio 2/3
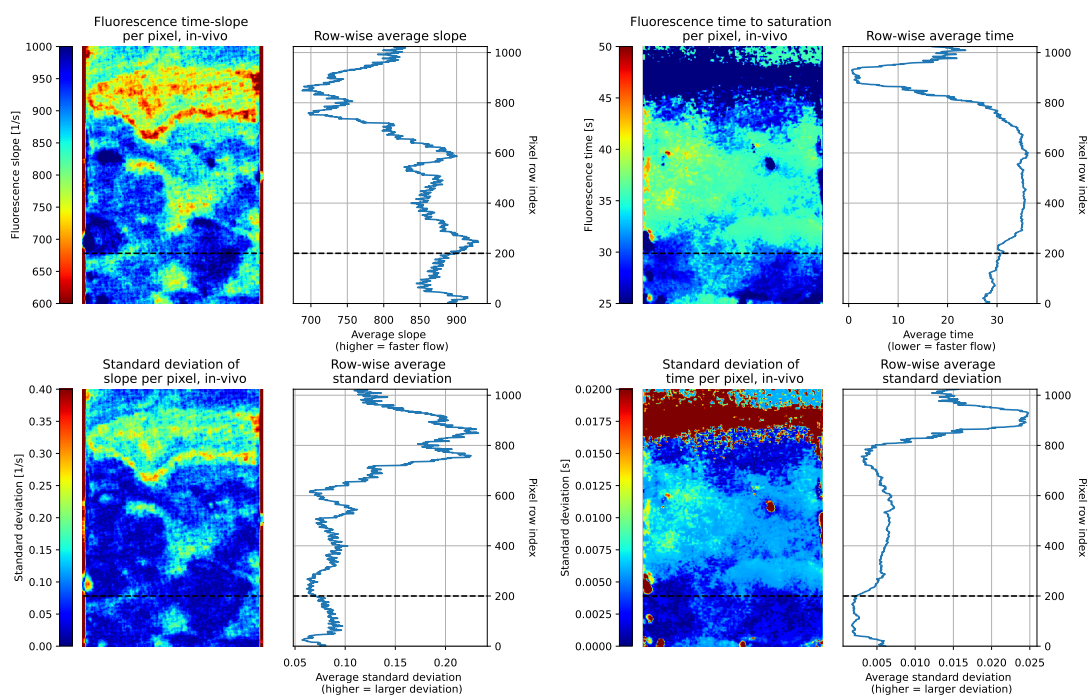
(a) Raw fluorescence slope images for the 2/3 devascularized porcine model. Anastomosis located at pixel row index 200.

(b) Raw absolute time images for the 2/3 devascularized porcine model. Anastomosis located at pixel row index 200.

Figure 6.2: The obtained results for the 2/3 de-vascularized anastomosis from the first ICG injection, i.e. the upper one in fig. 6.1.
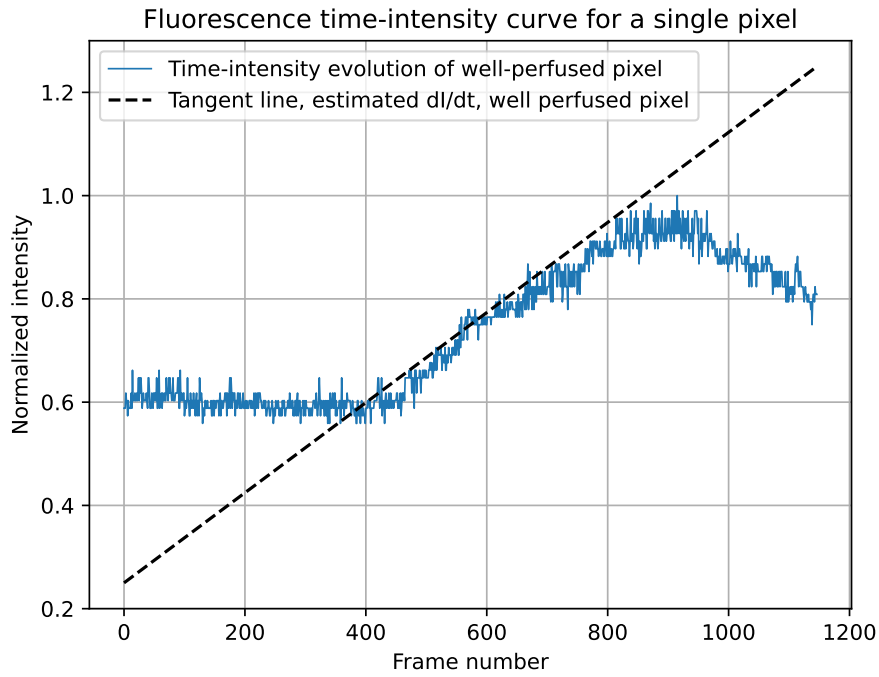
Figure 6.3: Evolution of the fluorescence signal for a single pixel in fig. 6.2(a) with numerically estimated derivative in the same pixel.

6.3.2   Anastomosis 2, de-vascularization ratio 1/3
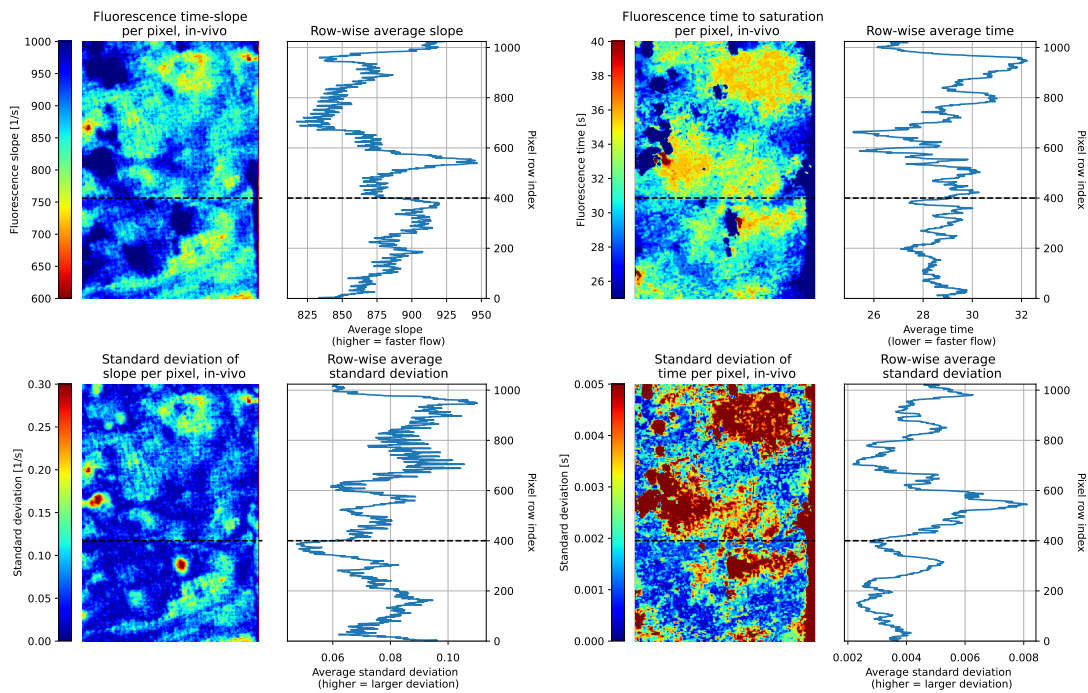
(a) Raw fluorescence slope images for the 1/3 de-vascularized porcine model. Anastomosis located at pixel row index 400.

(b) Raw absolute time images for the 1/3 de-vascularized porcine model. Anastomosis located at pixel row index 400.

Figure 6.4: The obtained results for the 1/3 de-vascularized anastomosis from the first ICG injection, i.e. the upper one in fig. 6.1.

6.4 Results, injection 2

6.4.1 Anastomosis 1, de-vascularization ratio 2/3
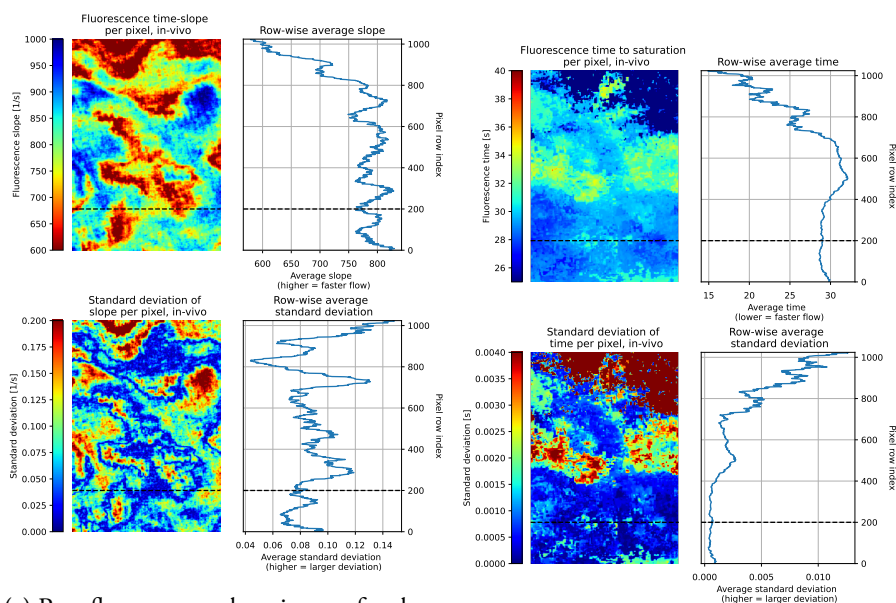
(a) Raw fluorescence slope images for the 2/3 de-vascularized porcine model. Anastomosis located at pixel row index 200.

(b) Raw absolute time images for the 2/3 de-vascularized porcine model. Anastomosis located at pixel row index 200.

Figure 6.5: The obtained results for the 2/3 de-vascularized anastomosis from the second ICG-injection, i.e. the upper one in fig. 6.1.

6.4.2 Anastomosis 2, de-vascularization ratio 1/3
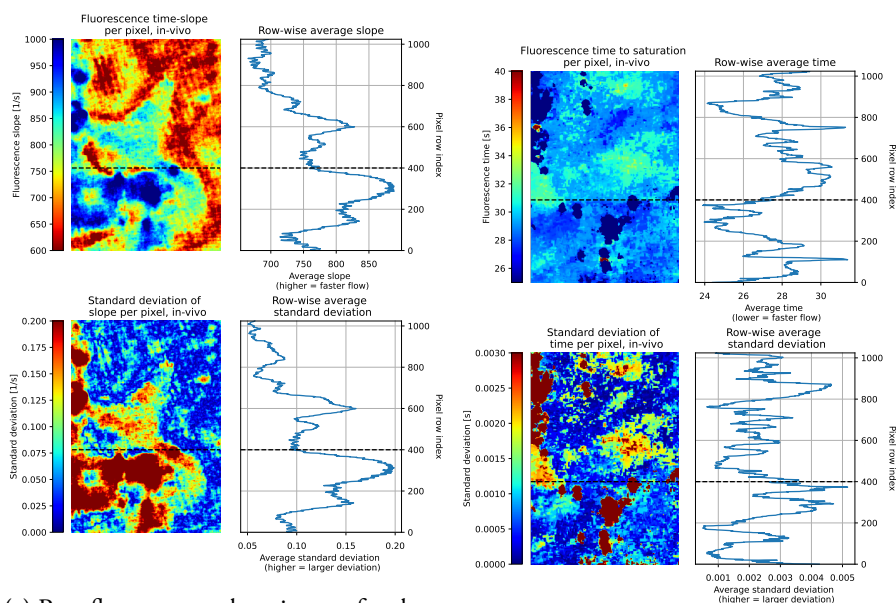
(a) Raw fluorescence slope images for the 1/3 de-vascularized porcine model. Anastomosis located at pixel row index 400.

(b) Raw absolute time images for the 1/3 de-vascularized porcine model. Anastomosis located at pixel row index 400.

Figure 6.6: The obtained results for the 1/3 de-vascularized anastomosis from the second ICG injection, i.e. the lower one in fig. 6.1.

6.5   Discussion

6.5.1   Injection 1

Beginning with the results in fig. 6.2, i.e. the 2/3 de-vascularization ratio anastomosis, it is clear that both algorithms display the same trend. There is a clear contrast in both images between the area below the anastomosis, which was well perfused and the area above it, where the perfusion speed was limited.

In the absolute time image, the general trend is very clear up to pixel row 800. Above this row, something interesting happens: the fluorescence slope algorithm indicates very poor perfusion in this area, which is also strengthened by its standard deviation plot as this is the area where it is the greatest (see fig. 6.2a.)). This should also indicate a very long time to saturation, but the corresponding area in fig. 6.2b.) shows the contrary. The conclusion is something which poses a big possible disadvantage with the absolute time algorithm: if a region of pixels is so poorly perfused that it never reaches saturation intensity, and rather stay essentially the same as at the start of the recording, they will have reached their maximum intensity almost instantly. Such a region is as such displayed in exactly the same way as a very well perfused one which reaches saturation intensity very quickly. The derivate approach of course alleviates this, as it distinguishes between a steep slope and a close to constant one. Furthermore, this displays a use case for the standard devation as a verification metric. The area in question is highlighted as highly red as it deviates highly from the surroundings. Other small patches which are similar in their value can easily be disregarded as artifacts. It is easily to correlate the two areas by eye and draw the conclusion that if there is such a sharp deviation in the trend as in fig. 6.2b.) over a large area, this rather indicates poor perfusion than an extremely well perfused area.

There is an inherent patchiness in the produced figures. Patches of poor perfusion appear in the well perfused area below the anastomosis, and vice versa. It is suggested that this may have arisen due to the complex and to the group, somewhat unknown at the time arterial network supplying the small intestine in pigs. Even though a blood vessel is located at the side where one wants to limit blood flow it may still later branch to other areas of the tissue. As such, patches of both types may arise and this could also be expected in humans. An idea to alleviate this could be to perform fluorescence angiography of the arterial network in conjunction with the production of these results. By visualizing the blood vessels themselves and correlating over areas of different perfusion, one could determine why the patchiness arises in a well substantiated way.

Continuing with the second anastomosis which was more vascularized than the first, i.e. the results displayed in fig. 6.4, it is clear that both algorithms reflect a higher degree of good blood flow to both sides of the anastomoses. Both the absolute time and fluorescence slope figures display a much more homogenous trend throughout the tissue. One can however still distinguish that above the anastomosis, the number of areas which tend toward a slower evolution is greater than below it. This is once again mainly revealed by the fluorescence slope algorithm, which once again highlights individual discrepancies rather than the general trend. In the case of fig. 6.4b.) the same trend is shown but harder to make out. The standard deviation once again proves worthwile when interpreting the absolute time image as it increases the contrast between areas of poor and rich perfusion respectively.

6.5.2   Injection 2

The second injection was performed after a downtime period of around 30 minutes, to allow the ICG to flush and exit the bloodstream hepatically. This was not verified quantitatively, and there may as such have been some initial fluorescence at the time of injection. The reason for this is two fold: firstly, it was hard to verify with the toolset available to us during the experiment. Secondly, it provides yet another test for

the algorithms as it would indicate if they are sensitive to this. In medical conditions it would not always be possible to know for sure if the fluorophore has been completely cleared if one performs several injections. One would likely work in a similar way to what was done here with allowing a somewhat arbitrary downtime between the injections.

The results obtained from the first anastomosis with 2/3 ratio (fig. 6.5) mimic the trends presented from the previous, albeit with a larger number of areas taking on values which are smaller than the lowest value in the colormap normalization (a slope of 600 s^{-1}). This can explained by the simple fact that the recording in this case was longer than the first (53 and 82 seconds respectively). The outcome of this is positive rather than negative, as it provides a better granularity between the pixels themselves. A longer recording holds more data on when pixels reached saturation which is reflected in the final figure. The resulting increase in contrast may be further revealed by adapting the normalization of the colormap, something which could prove worthwile in future developments where one might want to study individual focalities in the blood perfusion of a patient rather than display the general trend in the tissue. For the purposes of this report, the same normalization still holds, however.

The fact is also reflected in fig. 6.5b.) where at least a certain number of pixels in the pixel region above row 800 actually reached saturation, alleviating the aforementioned issue of pixels which fluoresced quickly appear the same as pixels which never reached saturation in the time span of the recording. The conclusion is that, to alleviate this problem completely, one would have to decide on a statistically substantiated standard recording length, which likely allows all pixels to reach saturation.

Furthermore, the results were not greatly affected by the possibility of fluorophore still being present in the tissue at the time of injection. The images display exactly the same trends as in the corresponding previous section, which is what is physiologically expected. To say for sure if the flushing downtime affect the results greatly, more tests would have to be performed. The naive conclusion is however that it does not affect the outcome greatly.

All of the above can also be said for fig. 6.6, the 1/3 ratio anastomosis.

It is clear that a greater recording length also affects the standard deviation plots, where the standard deviations seem somewhat amplified. This is however completely reasonable as the same physiologically motivated values of μ were used in these cases. A longer recording length will allow more pixels to deviate from these values than in the other case. This outcome is not necessarily a positive aspect, as it does not bring a lot to the table, more so than possible confusion for the person interpreting the images.

Chapter 7

Outlook

The work presented in this thesis has dealt with the development of simulations and image analysis algorithms to analyze indocyanine-green fluorescence in the context of esophagectomies and their possibility to lead to anastomotic leakages. The purpose of the work was to work toward a full and complete setup to measure blood perfusion in the anastomotic area, as this is theorized to be one of the main factors contributing to anastomotic leaks. Furthermore, experiments have been performed both in- and ex-vivo, on a porcine model of the thoracic situation after an esophagectomy, and in tissue phantoms respectively. The results obtained in these were analyzed using the aforementioned image analysis algorithms, that approach the same problem in two different ways. These were initially verified using the Monte-Carlo simulation model, to see if they at all could visualize differences in the time evolution, with conditions similar to the ones found in esophageal/ventricular tissue.

7.1 The thesis work

Two Monte-Carlo simulations of the collected fluorescence light distribution were performed, which provide recordings which were highly similar to the ones obtained during the in-vivo experiments, indicating that the assumptions and conditions were correctly estimated. Furthermore, the image analysis algorithms succeed in identifying discrepancies in the blood perfusion, both simulated and in tissue phantoms. The experiments regarding the latter indicate that the two algorithms may have different usecases depending on the patient-to-patient perfusion conditions: the absolute time approach highlights slow evolutions well, where the slope of the fluorescence may be close to constant throughout. Similarly the fluorescence slope approach highlights fast evolutions, where the absolute time algorithm is less well suited. The conclusion is that the algorithms may either be applied selectively in different regions of the tissue, or that they simply serve different usecases and should ideally be used together.

The in-vivo experiments involved two modeled anastomoses, sewn in the small intestine of a pig. The blood supply to the region above and below it was modulated, such that the area below was left untouched, simulating the human esophagus and the region above had a certain number of blood vessels clipped such that the perfusion speed was limited.

The image analysis algorithms were further tested on these, leading to a few important conclusions. The results from the absolute time algorithm can be misleading if perfusion is highly limited in a certain area of the tissue, such that it does not reach saturation during the time of recording. This issue can however be alleviated by recording for longer, to allow all pixels to reach saturation, and by including and interpreting the standard deviation from the physiological well-perfused mean, for each tissue. This does not arise

with the fluorescence slope algorithm, which also indicates individual focalities much better, something displayed by the patchiness in these images due to the complex blood supply in the imaged area. In conclusion, both of the algorithms should be used in conjunction to provide doctors with a full picture of the perfusion in to and from the anastomotic area.

It is worth noting that the perfusion throughout the tissue was not validated using established methods. This would be a necessary step if the developed algorithms are to be used clinically. Even though the algorithms provide the picture we expect, it would be highly necessary to validate the results as this would provide further clues toward if the algorithms show true discrepancies in the perfusion. This could for example be done using laser speckle contrast imaging, a method which has been explored for perfusion speed measurements like these to a high degree (see for example [5] for a description of the technique).

7.2   Future work: towards a full gastroscopy setup for ICG measurements

In the beginning of this thesis work, the plan was to, in contrast to the above, develop an instrument which could be used in gastroscopies of the anastomotic area. Even though a substantial amount of work towards this was done, it is not presented here as it never left the planning stage. This is mainly due to difficulties with the imaging capabilities of clinically used gastroscopes, as well as due to the secretive nature of their design.

A gastroscopy is a procedure where an endoscope is used to image the upper gastrointestinal tract of a patient. Endoscopes are long and narrow tubular devices, which contain a light source and some type of viewing optics, nowadays most commonly a camera. Most clinically used endoscopes contain a narrow working channel (typically 2-3 mm in diameter) in which medical devices can be inserted that may then be used during the gastroscopy.
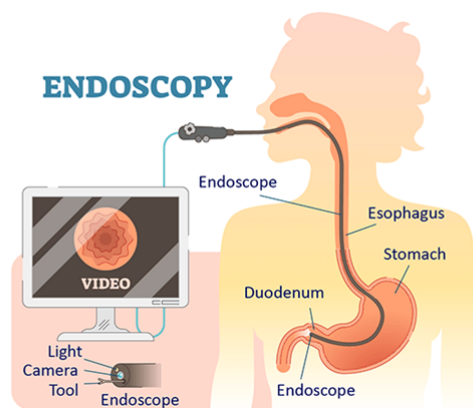
Figure 7.1: An illustration of the gastroscopy procedure, indicating the endoscope and how it is inserted into the patient. [22]

Post-esophagectomy, the imaging of the anastomotic area would of course have to be done in this way. This could be combined with an instrument which could be inserted into the working channel of the endoscope, containing the excitation light source as well as imaging optics for recording the fluorescence. It was found during the course of the thesis work that the endoscopes used at the Lund university hospital either contain a strong IR-filter or are not sensitive to infrared light at all. As such, the build in camera can in most cases not be used to image fluorescence without modification, something which, due to industrial secrecy, could only be done in cooperation with an endoscope manufacturer. This is most likely the reasonable approach, as it was found during the course of the thesis work that a small enough infrared camera of high quality, which could fit in the working channel together with a fiber coupled light source, is extremely

hard to find. As such, a proposed design would be to remove the IR-filter/modify the camera such that it is IR-sensitive. To simultaneously obtain an optical image, one could modulate the excitation light source with a rate of for example, the frame rate of the camera. Half of the recorded frames would then be the raw image, whereas half would record the fluorescence induced from the excitation light source. One could then extract these for processing with the developed algorithms. This approach could alleviate filtering the signal, which in turn requires a separate camera for the optical images (as in this thesis).

In conclusion, this work provides a clear proof of concept of how ICG-fluorescence can be quantified using different image analysis algorithms. This has been done specifically with anastomotic conditions after esophagectomies in mind. The work provides the first stepping stone toward future studies which should be focused on making the measurements applicable in practice.

Bibliography

[1]   Oscar Åkesson et al. "Early endoscopic assessment after esophagectomy can predict anastomotic complications: a novel scoring system". PhD thesis. Lund: Clinical sciences, Lund university, Mar. 2021. DOI: 10.1007/S00464-021-08472-4.

[2]   Jarmo T. Alander et al. *A Review of indocyanine green fluorescent imaging in surgery.* 2012. DOI: 10.1155/2012/940585.

[3]   Bruce Alberts. *Essential Cell Biology.* 5th ed. WW Norton & Co, 2018.

[4]   Adrian Barbu and Song Chun Zhu. *Monte carlo methods.* Springer Singapore, Jan. 2020, pp. 1–422. ISBN: 9789811329715. DOI: 10.1007/978-981-13-2971-5/COVER.

[5]   Johanna V Berggren et al. "Laser Speckle Contrast Imaging of the Blood Perfusion in Glabellar Flaps Used to Repair Medial Canthal Defects". In: *Ophthalmic Plastic & Reconstructive Surgery* 38.3 (2022). ISSN: 0740-9303. URL: https://journals.lww.com/op-rs/fulltext/2022/05000/laser_speckle_contrast_imaging_of_the_blood.10.aspx.

[6]   Walter F. Boron and Emile L. Boulpaep. *Medical Physiology.* 3rd. Elsevier, Mar. 2016. ISBN: 9781455733286. URL: https://doctorlib.info/physiology/medical/256.html.

[7]   Caroline Boudoux. *Fundamentals of biomedical optics : from light interactions with cells to complex imaging systems.* 2016, p. 428. ISBN: 1366446194. URL: https://books.google.com/books/about/Fundamentals_of_Biomedical_Optics.html?hl=sv&id=6yPCAQAACAAJ.

[8]   Janusz M. Dabrowski et al. "Engineering of relevant photodynamic processes through structural modifications of metallotetrapyrrolic photosensitizers". In: *Coordination Chemistry Reviews* 325 (Oct. 2016), pp. 67–101. ISSN: 0010-8545. DOI: 10.1016/J.CCR.2016.06.007.

[9]   Arthur F. Dalley and Anne M. R. Agur. *Moore's Clinically Oriented Anatomy.* 9th ed. Wolters Kluwer Health, Dec. 2021. ISBN: 9781975154080. URL: https://www.google.se/books/edition/Moore_s_Clinically_Oriented_Anatomy/SHhTEAAAQBAJ?hl=en.

[10]   Vincent T. DeVita, Theodore S. Lawrence, and Steven A. Rosenberg. *DeVita, Hellman, and Rosenberg's cancer: Principles & practice of oncology.* Wolters Kluwer Health Pharma Solutions (Europe) Ltd, Nov. 2018, pp. 1–2390. ISBN: 9781496394644.

[11]   *File:Diagram showing before and after a total oesophagectomy CRUK 105.svg - Wikimedia Commons.* URL: https://commons.wikimedia.org/wiki/File:Diagram_showing_before_and_after_a_total_oesophagectomy_CRUK_105.svg.

[12] *File:GI normal.jpg - Wikimedia Commons*. URL: `https://commons.wikimedia.org/wiki/File:GI_normal.jpg`.

[13] *File:Indocyanine green.png - Wikimedia Commons*. URL: `https://commons.wikimedia.org/wiki/File:Indocyanine_green.png`.

[14] *File:LDHvsICG (cropped).jpg - Wikimedia Commons*. URL: `https://commons.wikimedia.org/wiki/File:LDHvsICG_(cropped).jpg`.

[15] C.J. Foot. "Atomic Physics - C.J. Foot - Oxford University Press". In: *Oxford University Press* (2004). URL: `https://global.oup.com/academic/product/atomic-physics-9780198506966`.

[16] HyperPhysics. *Properties of molecules*.

[17] *Intel® Core™ i5-4590S Processor*. URL: `https://www.intel.com/content/www/us/en/products/sku/80816/intel-core-i54590s-processor-6m-cache-up-to-3-70-ghz/specifications.html`.

[18] *ISO/IEC 9899:2018 - Information technology — Programming languages — C*. URL: `https://www.iso.org/standard/74528.html`.

[19] *Ivor Lewis Esophagectomy | Stanford Health Care*. URL: `https://stanfordhealthcare.org/medical-treatments/e/esophagectomy/types/ivor-lewis-esophagectomy.html`.

[20] Sanne M. Jansen et al. "Feasibility of Optical Coherence Tomography (OCT) for Intra-Operative Detection of Blood Flow during Gastric Tube Reconstruction". In: *Sensors (Basel, Switzerland)* 18.5 (May 2018). ISSN: 14248220. DOI: 10.3390/S18051331. URL: `/pmc/articles/PMC5982600/%20/pmc/articles/PMC5982600/?report=abstract%20https://www.ncbi.nlm.nih.gov/pmc/articles/PMC5982600/`.

[21] Jan Johansson. *Nationellt kvalitetsregister för matstrups- och magsäckscancer (NREV) - RCC*. URL: `https://cancercentrum.se/samverkan/cancerdiagnoser/matstrupe-och-magsack/kvalitetsregister/`.

[22] John Hopkins University. *Upper GI Endoscopy*.

[23] Joakim Jönsson and Edouard Berrocal. "Multi-Scattering software: part I: online accelerated Monte Carlo simulation of light transport through scattering media". In: *Optics Express, Vol. 28, Issue 25, pp. 37612-37638* 28.25 (Dec. 2020), pp. 37612–37638. ISSN: 1094-4087. DOI: 10.1364/OE.404005. URL: `https://opg.optica.org/viewmedia.cfm?uri=oe-28-25-37612&seq=0&html=true%20https://opg.optica.org/abstract.cfm?uri=oe-28-25-37612%20https://opg.optica.org/oe/abstract.cfm?uri=oe-28-25-37612`.

[24] Brian Kernighan and Dennis Ritchie. *The C programming language*. 2nd ed. 1988.

[25] Anna Löfgren et al. "Hospital costs and health-related quality of life from complications after esophagectomy". In: *European Journal of Surgical Oncology* 47.5 (May 2021), pp. 1042–1047. ISSN: 0748-7983. DOI: 10.1016/J.EJSO.2020.09.032. URL: `https://portal.research.lu.se/en/publications/hospital-costs-and-health-related-quality-of-life-from-complicati`.

[26] Chia Hung Lu and Jong Kai Hsiao. "Indocyanine green: An old drug with novel applications". In: *Tzu-Chi Medical Journal* 33.4 (Oct. 2021), p. 317. ISSN: 10163190. DOI: `10.4103/TCMJ.TCMJ{\_}216{\_}20`. URL: `/pmc/articles/PMC8532591/%20/pmc/articles/PMC8532591/?report=abstract%20https://www.ncbi.nlm.nih.gov/pmc/articles/PMC8532591/`.

[27] Mikael Häggström. *File:Stomach blood supply.svg - Wikimedia Commons*.

[28] *Multi-Scattering*. URL: `https://multi-scattering.com/`.

[29] *OpenMP*. URL: `https://www.openmp.org/`.

[30] "Pointers on Installing the New Fluorescent Lamps". In: *Popular Science* (Jan. 1940), pp. 136–138. URL: `https://books.google.se/books?id=1iYDAAAAMBAJ&dq=popular+science+January+1940&pg=PA136&redir_esc=y#v=onepage&q=popular%20science%20January%201940&f=false`.

[31] William H. Press et al. *Numerical Recipes 3rd Edition: The Art of Scientific Computing*. 3rd. Vol. 1. Cambridge University Press, Sept. 2007. ISBN: 0521880688. URL: `http://www.amazon.com/Numerical-Recipes-3rd-Edition-Scientific/dp/0521880688?SubscriptionId=0JYN1NVW651KCA56C102&tag=techkie-20&linkCode=xm2&camp=2025&creative=165953&creativeASIN=0521880688`.

[32] Michaela B. Reinhart et al. "Indocyanine Green :Historical Context, Current Applications, and Future Considerations". In: *Surgical Innovation* 23.2 (Apr. 2016), pp. 166–175. ISSN: 15533514. DOI: `10.1177/1553350615604053`.

[33] Anthony S. Fauci et al. *Harrison's Principles of Internal Medicine*. Ed. by Anthony S. Fauci et al. 19th. 9. McGraw-Hill Education, Apr. 2015. ISBN: 9780071802161. DOI: `10.1017/CBO9781107415324.004`.

[34] Bahaa E. A. Saleh and Malvin Carl Teich. *Fundamentals of Photonics*. Wiley Series in Pure and Applied Optics. New York, USA: John Wiley & Sons, Inc., Aug. 1991. ISBN: 0471839655. DOI: `10.1002/0471213748`. URL: `https://onlinelibrary.wiley.com/doi/book/10.1002/0471213748`.

[35] David J. Sugarbaker et al. *Adult Chest Surgery*. 2nd ed. Houston: McGraw Hill, July 2014. ISBN: 9780071781909. URL: `https://www.google.se/books/edition/Adult_Chest_Surgery_2nd_edition/bTtIBQAAQBAJ?hl=en&gbpv=0&bsq=inauthor:%22David%20J.%20Sugarbaker%22`.

[36] Sune Svanberg. *Atomic and Molecular Spectroscopy*. 4th ed. Advanced Texts in Physics. Berlin, Heidelberg: Springer Berlin Heidelberg, 2004. ISBN: 978-3-540-20382-7. DOI: `10.1007/978-3-642-18520-5`. URL: `https://link.springer.com/10.1007/978-3-642-18520-5`.

[37] Nermin Topaloglu, Murat Gulsoy, and Sahru Yuksel. "Antimicrobial Photodynamic Therapy of Resistant Bacterial Strains by Indocyanine Green and 809-nm Diode Laser". In: *Photomedicine and laser surgery* 31 (Jan. 2013). DOI: `10.1089/pho.2012.3430`.

[38] Valery V. Tuchin. *Tissue optics: Light scattering methods and instruments for medical diagnosis: Third edition*. SPIE, Feb. 2015, pp. 1–935. ISBN: 9781628415179. DOI: `10.1117/3.1003040`.

[39]   Lihong Wang, Steven L. Jacques, and Liqiong Zheng. "MCML—Monte Carlo model-
         ing of light transport in multi-layered tissues". In: *Computer Methods and Programs in
         Biomedicine* 47.2 (July 1995), pp. 131–146. ISSN: 0169-2607. DOI: `10 . 1016 / 0169 -
         2607(95)01640-F`.

[40]   *What are optical brighteners in laundry detergent⊠ - Raytop Chemical*. URL: `https://www.
         raytopoba.com/What-are-optical-brighteners-in-laundry-detergent_
         170.html`.

[41]   *Why does tonic water glow?. A brief history of quinine… | by John Woodland | Medium*. URL:
         `https://jgwoodland.medium.com/why-does-tonic-water-glow-
         5354870892f3`.

[42]   Wikimedia Commons. *File:Animal cell structure en.svg - Wikimedia Commons*. URL: `https:
         //commons.wikimedia.org/wiki/File:Animal_cell_structure_en.svg`.

Appendix A

Simulation code

A.1   Header files and their implementations

A.1.1   RandChoice.c

```c
#include <stdlib.h>
#include "RandChoice.h"

float randChoice(float *randlist, float *weights, int len) {
    /*
    Generate weighted random numbers by calculating the cumulative
    sum of the weights and finding the weight which is greater or
    equal to the generated random number.

    Arguments:
    *randlist: array of floats containing numbers to choose from.
    *weigths: array of floats containing the weight of each number
    in the distribution. Must be indexed and equal in length to
    randlist.
    len: the length of the arrays.

    Returns:
    A weigthed random pick.
    */
    int low = 0;
    int mid = 0;
    float wsum = 0;
    float *cweights = calloc(len, sizeof(float));
    //Calculate cumulative sums of weights
    if (cweights == NULL) {
        return -1;
    } else {
        for (int i = 0; i < len; i++) {
            wsum += weights[i];
            cweights[i] = wsum;
        }
    };
    //Generate a random number between 0 and wsum
    float rnd = ((float)rand()/(RAND_MAX))*wsum;
    //Find the weighted choice by binary search
    while (low < len) {
        mid = (low + len - 1)/2;
        if (rnd == cweights[mid]) {
            break;
        } else if (rnd > cweights[mid]) {
            low = mid + 1;
        } else {
            len = mid - 1;
```

```
            }
    };

    free(cweights);

    return randlist[mid];
};
```

A.1.2   ddHist.c

```c
#include "ddHist.h"
/*
Author: Love Kildetoft
*/
void genBinEdges(float *lbin_edge, float *hbin_edge, float low, float high, int nbins) {
    float width = (high - low)/nbins;
    float curr_bin = low;
    for (int i = 0; i < nbins; i++) {
        lbin_edge[i] = curr_bin;
        hbin_edge[i] = curr_bin + width;
        curr_bin += width;
    }
};

void genHist(int **hist, float *rl_edges, float *rh_edges, float *cl_edges, float *ch_edges,
    int nrows, int ncols, float x, float y) {
    int row_idx, col_idx;

    for (int i = 0; i < nrows; i++) {
        float curr_row_l = rl_edges[i];
        float curr_row_h = rh_edges[i];

        for (int j = 0; j < ncols; j++) {
            float curr_col_l = cl_edges[j];
            float curr_col_h = ch_edges[j];
            int row_cond = 0;
            int col_cond = 0;

            if ((y > curr_row_l) && (y < curr_row_h)) {
                row_idx = i;
                row_cond = 1;
            }

            if ((x > curr_col_l) && (x < curr_col_h)) {
                col_idx = j;
                col_cond = 1;
            }

            if ((y == curr_row_l) && (i != 0)) {
                row_idx = i - 1;
                row_cond = 1;
            }

            if ((y == curr_row_h) && (j != (nrows - 1))) {
                row_idx = i + 1;
                row_cond = 1;
            }

            if ((x == curr_col_l) && (j != 0)) {
                col_idx = j - 1;
                col_cond = 1;
            }

            if ((x == curr_col_h) && (j != (ncols - 1))) {
                col_idx = j + 1;
                col_cond = 1;
            }

            if ((row_cond == 1) && (col_cond == 1)) {
                hist[row_idx][col_idx] += 1;
```

```
            }
        }
    }
};
```

A.1.3 Distrs.c

```c
#include "Distrs.h"
#include <math.h>
#include <stdio.h>

/*
Author: Love Kildetoft
*/
//Everyones favourite numerical constant
const float pi = 3.141592653589793;

float phaseFunc(float theta, float g) {
    /*
    Henvey-Greenstein scattering phase function.

    Arguments:
    theta: angle in radians. Range depends on coordinate
    system.
    g: anisotropy factor of medium, between -1 and 1.

    Returns:
    Value of the scattering phase function at theta, g.
    */
    float p = (float)((1/(4*pi))*((1-pow(g, 2))/(pow(1+pow(g, 2)-2*g*cos(theta), 3/2))));
    return p;
};

float flowGrad(float idx, float max_idx, float max_conc, float max_low, float grad_low, float
    high_factor) {
    float grad;
    if (idx > max_idx) {
        grad = high_factor;
    } else if (idx < max_idx) {
        if ((max_low - grad_low*(idx/max_idx) >= 0)) {
            grad = max_low*(1- grad_low*(idx/max_idx));
        } else {
            grad = 0;
        }
    };
    return grad;
}

float expFunc(float x, float mue) {
    /*
    Exponentially decaying distribution (see Beer-Lambert law).
    */
    float p = (float)(mue*exp(-mue*x));
    return p;
};
```

A.1.4 Simulation.c

```c
/*
Author: Love Kildetoft
*/
#include <math.h>
#include <stdlib.h>

#include "Distrs.h"
#include "RandChoice.h"
#include "Simulation.h"
```

```c
void genPhaseVals(float *plist, int size, float lim, float g) {
    /*
    Modify an empty float array to contain scattering phase function
    values.
    */
    int n = 0;
    for (float i = -1 * lim; i < lim; i += (2 * lim / size)) {
        plist[n++] = phaseFunc(i, g);
    };
};

void genUniform(float *ulist, int nvals) {
    /*
    Just the same value over and over. In statistics we call it a
    uniform distribution :D
    */
    for (int i = 0; i < nvals; i++) {
        ulist[i] = (float)1/nvals;
    };
};

void interact(photon *p, esophagus *eso, indocyn *icg, float conc, float *t_angles, float *
    t_phasevals, int len) {
    /*
    Simulates the interaction of photons in a medium with appropriate parameters.
    A "photon" is absorbed and scattered at each call.
    */
    float w = p->w;
    //Account for a certain concentration of ICG in the tissue
    float choices[2] = {0, 1};
    float choice_prob[2] = {conc, 1.0-conc};

    float mua;
    float mus;
    //Find the appropriate coefficients
    int choice = randChoice(choices, choice_prob, 2);
    if (choice == 0) {
        mua = icg->mua;
        mus = icg->mus;
        p->curr_abs = 1;
    } else {
        mua = eso->mua_ex;
        mus = eso->mus_ex;
        p->curr_abs = 0;
    };

    float mue = mua + mus;
    float l;
    //Calculate new path from angles and randomly generated path length
    float theta = randChoice(t_angles, t_phasevals, len);
    float phi = 2*pi*((float)rand()/(float)RAND_MAX);
    float path = (float)rand()/(float)RAND_MAX;
    if (path == 0) {
        l = 0;
    } else {
        l = -1*log(path)/(mue);
    }
    float xs = l*sin(theta)*cos(phi);
    float ys = l*sin(theta)*sin(phi);
    float zs = l*cos(theta);
    //Update the weight and coordinates of the photon
    p->w -= (mua/mue)*w;
    p->x += xs;
    p->y += ys;
    p->z += zs;
};

void fluoress(photon *p, esophagus *eso, indocyn *icg, float conc, float *t_angles, float *
    t_phasevals, int len) {
    /*
    Simulates the interaction of photons in a medium with appropriate parameters.
    A "photon" is absorbed and scattered at each call.
```

```c
    */
    float w = p->w;
    //Account for a certain concentration of ICG in the tissue
    float choices[2] = {0, 1};
    float choice_prob[2] = {conc, 1.0-conc};

    float mua;
    float mus;
    //Find the appropriate coefficients
    int choice = randChoice(choices, choice_prob, 2);
    if (choice == 0) {
        mua = icg->mua;
        mus = icg->mus;
        p->curr_abs = 1;
    } else {
        mua = eso->mua_fl;
        mus = eso->mus_fl;
        p->curr_abs = 0;
    };

    float mue = mua + mus;
    float l;
    //Calculate new path from angles and randomly generated path length
    float theta = randChoice(t_angles, t_phasevals, len);
    float phi = 2*pi*((float)rand()/(float)RAND_MAX);
    float path = (float)rand()/(float)RAND_MAX;
    if (path == 0) {
        l = 0;
    } else {
        l = -1*log(path)/(mue);
    }
    float xs = l*sin(theta)*cos(phi);
    float ys = l*sin(theta)*sin(phi);
    float zs = l*cos(theta);
    //Update the weight and coordinates of the photon
    p->w -= (mua/mue)*w;
    p->x += xs;
    p->y += ys;
    p->z += zs;
};
```

A.2   Main function

```c
/*
ICG-SIM: A Monte-Carlo simulation of light propagation and fluorescence from
indocyanine-green (ICG) in tissues. Can easily be modified for other fluorophores.
Specifically developed to simulate mal-perfusion in the anastomosis after esophagectomy,
as such allows for three distinct areas with ICG-concentrations growing at different speeds.

Author: Love Kildetoft

Based on MCML by Steven Jaques et. al. and its extension to simulate
fluorescence, but written and adapted from scratch.
Saves the current "face" and depth image of the absorbed and fluorescence
photons at each iteration. These files may become very large in the end
depending on the amount of photons/iterations/binning, so tread
carefully!

To run a simulation:
Right now, the parameters have to be modified directly in the main function. If
you strictly follow my guide here, nothing should break :) All are set to
appropriate defaults corresponding to the human esophagus.
After the parameters have been set, compile and run using your favourite
compiler!

Parameters:
    int niters: total number of iterations
    ****************************************************************************
    int nvals: the number of values (granularity/resolution) for the sim,
```

```c
      eg. the number of paths/angles/total grid on which the photons may
      propagate.
      ****************************************************************************
      int nphotons: total number of "photons" used in the simulation, usually
      a very large number.
      ****************************************************************************
      float ls_x: x-position of the light source
      float ls_y: y-position of the light source
      float ls_z: z-position of the light source
      float ls_sp_r: radial spread, a point source can be simulated by making
      this variable very small.
      ****************************************************************************
      float e_xmax: x-length of the tissue.
      float e_ymax: y-length of the tissue.
      float e_zmax: z-length of the tissue.
      float e_mus_ex: scattering coefficient of the tissue, for excitation photons.
      float e_mua_ex: absorption coefficient of the tissue, for excitation photons.
      float e_mus_fl: scattering coefficient of the tissue, for fluorescence photons.
      float e_mua_fl: absorption coefficient of the tissue, for fluorescence photons.
      ****************************************************************************
      float i_mus: scattering coefficient of indocyanine green.
      float i_mua: absorption coefficient of indocyanine green.
      ****************************************************************************
      float g_ex: overall anisotropy parameter for excitation photons.
      float g_fl: overall anisotropy parameter for fluorescence photons.
      ****************************************************************************
      float injected_conc: total "injected"/maximum ICG-concentration
      float mal_conc: initial concentration for mal-perfusive region.
      float icg_conc_upper: initial concentration above mal-perfusive region.
      float icg_conc_lower: initial concentration below mal-perfusive region.
      ****************************************************************************
      float mal_factor: ICG-concentration increase at each iteration, mal-perfusive
      region.
      float icg_upper_factor: ICG-concentration increase at each iteration, upper
      region.
      float icg_lower_factor: ICG-concentration increase at each iteration, lower
      region.
      ****************************************************************************
      float l_mal_area: lower z-bound for mal-perfusive region.
      float h_mal_area: upper z-bound for mal-perfusive region.
      ****************************************************************************
      float fl_ratio: 1 - probability for photon to undergo fluorescence by ICG.
      ****************************************************************************
      int nrows: number of rows in the output histograms/images.
      int ncols: number of columns in the output histograms/images.
      ****************************************************************************
      Good luck!
*/
#include <stdio.h>
#include <stdlib.h>
#include <time.h>
#include <string.h>
#include <math.h>
#include <omp.h>

#include "Distrs.h"
#include "Simulation.h"
#include "RandChoice.h"
#include "ddHist.h"

int main(int argc, const char * argv[]) {
    //Sim parameters, see above.
    //clock_t begin = clock();
    int niters = 5000;
    int nvals = 500;
    int nphotons = (int)1e8;

    float ls_x = 1;
    float ls_y = 0;
    float ls_z = 12.5;
    float ls_sp_r = 12.5;

    float e_xmax = 2;
```

```c
    float e_ymax = 2;
    float e_zmax = 5;
    float e_mus_ex = 29.5;
    float e_mua_ex = 3.3;
    float e_mus_fl = 33;
    float e_mua_fl = 3.3;

    float i_mus = 2.1;
    float i_mua = 209;

    float g_ex = 0.85;
    float g_fl = 0.8;

    float inj_conc = 0.25;
    float icg_upper_factor = 0.1;
    float icg_lower_factor = 0.001;

    int ana_idx = 24;

    int fl_ratio = 20;

    int nrows = 32;
    int ncols = 24;

    /*
    Here, the actual simulation starts and no more parameters should
    require modification.
    */
    lightsource *source = &(lightsource){ls_x, ls_y, ls_z, ls_sp_r};
    esophagus *eso = &(esophagus){e_xmax, e_ymax, e_zmax, e_mus_ex, e_mua_ex, e_mus_fl,
        e_mua_fl};
    indocyn *icg = &(indocyn){i_mus, i_mua};
    int npackets = nphotons/niters;
    float fl_choice[2] = {1, 0};
    float fl_prob[2] = {(float)(1 - 1/fl_ratio), (float)(1/fl_ratio)};
    //Seed random generator
    srand((unsigned)time(NULL));
    //Create output files and their corresponding file-pointers.
    FILE *frontFluor = fopen("front_fl_frames.txt", "w");
    FILE *frontAbs = fopen("front_abs_frames.txt", "w");
    FILE *depthFluor = fopen("depth_fl_frames.txt", "w");
    FILE *depthAbs = fopen("depth_abs_frames.txt", "w");
    //Allocate space in memory for everything needed for the sim
    photon *photons = calloc(nphotons, sizeof(photon));

    float *theta = calloc(nvals, sizeof(float));

    float *conc_arr = calloc(nrows, sizeof(float));

    float *t_plist_ex = calloc(nvals, sizeof(float));
    float *t_plist_fl = calloc(nvals, sizeof(float));

    float *rl_edges = calloc(nrows, sizeof(float));
    float *rh_edges = calloc(nrows, sizeof(float));
    genBinEdges(rl_edges, rh_edges, 0, eso->zmax, nrows);
    printf("Anastomosis located at %f cm", (rl_edges[ana_idx] + rh_edges[ana_idx])/2);
    float *cl_edges = calloc(nrows, sizeof(float));
    float *ch_edges = calloc(nrows, sizeof(float));
    genBinEdges(cl_edges, ch_edges, 0, eso->xmax, ncols);

    int **front_hist_fl = calloc(nrows, sizeof(int*));
    int **front_hist_abs = calloc(nrows, sizeof(int*));
    int **depth_hist_fl = calloc(nrows, sizeof(int*));
    int **depth_hist_abs = calloc(nrows, sizeof(int*));

    for (int i = 0; i < nrows; i++) {
        front_hist_fl[i] = calloc(ncols, sizeof(int));
        front_hist_abs[i] = calloc(ncols, sizeof(int));
        depth_hist_fl[i] = calloc(ncols, sizeof(int));
        depth_hist_abs[i] = calloc(ncols, sizeof(int));
    };
    //Fill scattering phase function arrays
    genPhaseVals(t_plist_ex, nvals, pi, g_ex);
```

```c
    genPhaseVals(t_plist_fl, nvals, pi, g_fl);
    //Fill polar angle array
    int k = 0;
    for (float i = -pi; i < pi; i+=(pi)/(float)nvals) {
        theta[k++] = i;
    };

    printf("Initializing %d photons, please wait \n", nphotons);
    //Fill photon array with appropriate homogenous distribution over the tissue surface.
    #pragma omp parallel for
    for (int i = 0; i < nphotons; i++) {
        float ang = 2*pi*((float)rand()/(float)RAND_MAX);
        float sp = (source->spread_r)*((float)rand()/(float)RAND_MAX);
        photons[i] = (photon){((source->x)+(sp)*cos(ang)), source->y, ((source->z) + (sp)*sin(
            ang)), 1.0, 0, 0, 0};
    };

    printf("Simulation started with %d photons, please wait \n", nphotons);
    //Main simulation loop
    int curr_iter_max = npackets;
    for (int iter = 0; iter < niters; iter++) {
        //Keep track of the number of absorbed/fluorescense photons each iteration.
        printf("Running simulation, %f %% done \n", ((float)iter/niters)*100);
        printf("Working on photons 0 to %d \n", curr_iter_max);
        //Update the ICG-concentration in each area
        for (int i = 0; i < nrows; i++) {
            if (conc_arr[i] < inj_conc) {
                conc_arr[i] += flowGrad(i, ana_idx, inj_conc, icg_lower_factor, 0.6,
                    icg_upper_factor);
            } else {
            }
        }
        //Loop over all photons
        #pragma omp parallel for
        for (int q = 0; q < curr_iter_max; q++) {
            photon *p;
            p = &photons[q];
            //Check fluorescence
            if ((p->w <= 0.1) && (p->outside == 0) && (p->curr_abs == 1)) {
                float fl_event = randChoice(fl_choice, fl_prob, 2);
                if (fl_event == 1) {
                    p->w = 1.0;
                    p->fluor = 1;
                }
            }
            //Let the current photon interact/fluoress appropriately depending on its current
                parameters
            if ((p->w > 0) && (p->outside == 0) && p->fluor == 0) {
                if (((p->x)*(p->x - eso->xmax) > 0) || ((p->y)*(p->y - eso->ymax) > 0) || ((p
                    ->z)*(p->z - eso->zmax) > 0)) {
                    p->outside = 1;
                } else {
                    for (int i = 0; i < nrows; i++) {
                        float curr_bin_l = rl_edges[i];
                        float curr_bin_h = rh_edges[i];
                        if ((p->z - curr_bin_l)*(p->z - curr_bin_h) <= 0) {
                            interact(p, eso, icg, conc_arr[i], theta, t_plist_ex, nvals);
                        }
                    }
                }
            } else if ((p->w > 0) && (p->outside == 0) && p->fluor == 1) {
                if (((p->x)*(p->x - eso->xmax) > 0) || ((p->y)*(p->y - eso->ymax) > 0) || ((p
                    ->z)*(p->z - eso->zmax) > 0)) {
                    p->outside = 1;
                } else {
                    for (int i = 0; i < nrows; i++) {
                        float curr_bin_l = rl_edges[i];
                        float curr_bin_h = rh_edges[i];
                        if ((p->z - curr_bin_l)*(p->z - curr_bin_h) <= 0) {
                            fluoress(p, eso, icg, conc_arr[i], theta, t_plist_fl, nvals);
                        }
                    }
                }
```

```c
            }

            //Generate histograms
            if ((p->w <= 0.1) && (p->outside == 0) && (p->curr_abs == 1) && (p->fluor == 0)) {
                genHist(front_hist_abs, rl_edges, rh_edges, cl_edges, ch_edges, nrows, ncols,
                    p->x, p->z);
                genHist(depth_hist_abs, rl_edges, rh_edges, cl_edges, ch_edges, nrows, ncols,
                    p->y, p->z);
            }

            if ((p->w > 0) && (p->fluor == 1) && (p->outside == 0) && (p->y <= 0.1)) {
                genHist(front_hist_fl, rl_edges, rh_edges, cl_edges, ch_edges, nrows, ncols, p
                    ->x, p->z);
                genHist(depth_hist_fl, rl_edges, rh_edges, cl_edges, ch_edges, nrows, ncols, p
                    ->y, p->z);
            }
        }
        //Write each histogram at each iteration to the appropriate file
        for (int row = 0; row < nrows; row++) {
            for (int col = 0; col < ncols; col++) {
                fprintf(frontFluor, "%d", front_hist_fl[row][col]);
                fprintf(depthFluor, "%d", depth_hist_fl[row][col]);
                fprintf(frontAbs, "%d", front_hist_abs[row][col]);
                fprintf(depthAbs, "%d", depth_hist_abs[row][col]);
                if (col < (ncols - 1)) {
                    fprintf(frontFluor, ",");
                    fprintf(depthFluor, ",");
                    fprintf(frontAbs, ",");
                    fprintf(depthAbs, ",");
                }
            }
            fprintf(frontFluor, "\n");
            fprintf(depthFluor, "\n");
            fprintf(frontAbs, "\n");
            fprintf(depthAbs, "\n");
        }
        curr_iter_max += npackets;
    }
    //Finished! Nice
    printf("Done \n");
    //clock_t end = clock();
    //double benchmark = (double)(end - begin) / CLOCKS_PER_SEC;
    //printf("%lf s", benchmark);
    //Free up memory
    fclose(frontFluor);
    fclose(frontAbs);
    fclose(depthFluor);
    fclose(depthAbs);

    free(photons);
    free(theta);
    free(t_plist_ex);
    free(t_plist_fl);
    for (int i = 0; i < nrows; i++) {
        free(front_hist_fl[i]);
        free(front_hist_abs[i]);
        free(depth_hist_fl[i]);
        free(depth_hist_abs[i]);
    };
    free(front_hist_fl);
    free(front_hist_abs);
    free(depth_hist_fl);
    free(depth_hist_abs);
    //Close all file-pointers


    return 0;
}
```

Appendix B

Implementations of the image analysis algorithms

B.1 Code to read movie files

```python
import cv2
import numpy as np
import matplotlib.pyplot as plt
import matplotlib as mlt
import itertools as it

def readmovie(fname: str) -> np.ndarray:
    """
    Reads a movie file and returns an array of frames, stored
    as multidimensional numpy arrays (pixel matrices) in a
    numpy array.

    Arguments:
        fname: str
        The name of the file you would like to parse. Must be an
        appropriate file format (eg. *.avi or similar).

    Returns:
        frames: np.ndarray
        Array containing each frame from the input file.
    """
    #Check for errors
    if isinstance(fname, str):
        vidcap = cv2.VideoCapture(fname)
        nframes = int(vidcap.get(cv2.CAP_PROP_FRAME_COUNT))
        frame_h = int(vidcap.get(cv2.CAP_PROP_FRAME_HEIGHT))
        frame_w = int(vidcap.get(cv2.CAP_PROP_FRAME_WIDTH))
        fps = float(vidcap.get(cv2.CAP_PROP_FPS))
        print(f"Image output will be {frame_h}*{frame_w} pixels")
    else:
        raise TypeError("fname is not a string")

    frames = np.fromiter((cv2.cvtColor(vidcap.read()[1], cv2.COLOR_BGR2GRAY) for i in range(
        nframes)), dtype = np.dtype(object, (nframes, frame_h, frame_w)), count = nframes)

    vidcap.release()
    #Check if parsing succeeded
    if len(frames) == 0:
        raise ValueError("Parsing did not succeed and an empty array was returned")
    else:
        print("Done")
        return frames, fps
```

B.2   Implementation of algorithm 1

```python
def gen_danger_matrix(framearr: np.ndarray, fps: float = 25) -> np.ndarray:
    """
    Generates a "danger area" from the input video where it takes a long time to
    reach peak pixel intensity

    Arguments:
    fname: str
    The name of the file you would like to parse. Must be an
    appropriate file format (eg. *.avi or similar).

    Returns:
    frames: np.ndarray
    Array containing each frame from the input file.
    """
    if len(framearr) != 0:
        if framearr[-1].ndim > 1:
            print("Calculating mask")
            mask = np.zeros(np.shape(framearr[-1]))
            for i in range(len(framearr)):
                mask[(framearr[i] >= framearr[-1]) & (mask == 0)] = i/fps
            mask[mask == 0] = len(framearr)/fps
        else:
            raise ValueError("Input frames are one dimensional, must be multidimensional")
    else:
        raise ValueError("frame array is empty")
    if not np.any(mask):
        raise ValueError("Mask was not filled and is empty")
    else:
        print("Done")
    return mask
```

B.3   Implementation of algorithm 2

```python
def gen_danger_matrix_deriv(framearr: np.ndarray, fps: float = 25) -> np.ndarray:
mask = []
for i in range(0, len(framearr) - 1):
    mask.append((framearr[i+1] - framearr[i])/((1/fps)))

mask = np.sum(mask, axis = 0)/len(mask)

return mask
```